doi:10.1016/j.jmb.2008.11.053 J. Mol. Biol. (2009) 385, 1221–1229

JMB

Available online at www.sciencedirect.com

ScienceDirect

ELSEVIER

Structure–Function Relationship of Tumor Necrosis Factor (TNF) and Its Receptor Interaction Based on 3D Structural Analysis of a Fully Active TNFR1-Selective TNF Mutant

Yohei Mukai[1,2], Hiroko Shibata[2], Teruya Nakamura[3], Yasuo Yoshioka[2,4], Yasuhiro Abe[2], Tetsuya Nomura[1,2], Madoka Taniai[5], Tsunetaka Ohta[5], Shinji Ikemizu[3], Shinsaku Nakagawa[1], Shin-ichi Tsunoda[2], Haruhiko Kamada[2], Yuriko Yamagata[3] and Yasuo Tsutsumi[1,2]*

[1]*Graduate School of Pharmaceutical Sciences, Osaka University, 1-6 Yamadaoka, Suita, Osaka 565-0871, Japan*

[2]*Laboratory of Pharmaceutical Proteomics, National Institute of Biomedical Innovation, Osaka 567-0085, Japan*

[3]*Graduate School of Pharmaceutical Sciences, Kumamoto University, Kumamoto 862-0973, Japan*

[4]*The Center for Advanced Research and Education in Drug Discovery and Development, Osaka University, 1-6 Yamadaoka, Suita, Osaka 565-0871, Japan*

[5]*Hayashibara Biochemical Laboratories, Inc., 1-2-3 Shimoishii, Okayama 702-8006, Japan*

Received 9 July 2008; received in revised form 21 November 2008; accepted 22 November 2008
Available online 6 December 2008

Edited by I. Wilson

Tumor necrosis factor (TNF) is an important cytokine that suppresses carcinogenesis and excludes infectious pathogens to maintain homeostasis. TNF activates its two receptors [TNF receptor (TNFR) 1 and TNFR2], but the contribution of each receptor to various host defense functions and immunologic surveillance is not yet clear. Here, we used phage display techniques to generate receptor-selective TNF mutants that activate only one TNFR. These TNF mutants will be useful in the functional analysis of TNFR.

Six amino acids in the receptor binding interface (near TNF residues 30, 80, and 140) were randomly mutated by polymerase chain reaction. Two phage libraries comprising over 5 million TNF mutants were constructed. By selecting the mutants without affinity for TNFR1 or TNFR2, we successfully isolated 4 TNFR2-selective candidates and 16 TNFR1-selective candidates, respectively. The TNFR1-selective candidates were highly mutated near residue 30, whereas TNFR2-selective candidates were highly mutated near residue 140, although both had conserved sequences near residues 140 and 30, respectively. This finding suggested that the phage display technique was suitable for identifying important regions for the TNF interaction with TNFR1 and TNFR2. Purified clone R1-6, a TNFR1-selective candidate, remained fully bioactive and had full affinity for TNFR1 without activating TNFR2, indicating the usefulness of the R1-6 TNF mutant in analyzing TNFR1 receptor function.

To further elucidate the receptor selectivity of R1-6, we examined the structure of R1-6 by X-ray crystallography. The results suggested that R31A and R32G mutations strongly influenced electrostatic interaction with TNFR2, and that L29K mutation contributed to the binding of R1-6 to TNFR1. This phage display technique can be used to efficiently construct functional mutants for analysis of the TNF structure–function relationship, which might facilitate *in silico* drug design based on receptor selectivity.

Keywords: TNF; X-ray crystallography; phage display system; TNF mutant; receptor specificity

**Corresponding author.* Department of Toxicology, Graduate School of Pharmaceutical Sciences, Osaka University, 1-6 Yamadaoka, Suita, Osaka 565-0871, Japan. E-mail address: ytsutsumi@phs.osaka-u.ac.jp.

Abbreviations used: TNF, tumor necrosis factor; TNFR, TNF receptor; SPR, surface plasmon resonance; wtTNF, wild-type TNF; PDB, Protein Data Bank.

Introduction

Tumor necrosis factor (TNF) is as an important immunity-modulating cytokine that is required for human body defense against infectious diseases and carcinogenesis.[1] Excess TNF, however, causes various autoimmune diseases, such as rheumatoid arthritis, Crohn's disease, and ulcerative colitis.[2–4] The relationship between TNF and disease deterioration must be unraveled before effective therapies can be developed. Both TNF receptor (TNFR) types TNFR1 and TNFR2, which induce different cell signaling, must be analyzed to better understand the function of TNF. Experiments with TNFR knockout mice have revealed the individual functions of TNFR1 and TNFR2 against viral infection, microbial pathogens, and tumor immunity.[5–8] The lack of one TNFR type, however, can affect the function of the other receptor type and weaken its signaling because the two receptors work together by crosstalk signaling.[9–11] This issue complicates investigations of the individual roles of TNFR1 and TNFR2, and the analysis of TNFR function. Therefore, many researchers have attempted to activate only one receptor using a receptor-selective TNF mutant that does not impair the function of the receptor.

In the past decade, several receptor-selective TNF mutants, which are useful for functional analysis of TNFRs, have been constructed.[12,13] Traditional point mutation methods, however, are labor-intensive because a large number of candidates must be individually assessed; therefore, it has been difficult to successfully isolate the desired mutants.[14–17] In particular, a receptor-selective TNF mutant with full bioactivity was difficult to develop due to the fact that a region on TNF shares a binding affinity for the two different receptors.[18,19] Furthermore, inadequate mutations cause a loss of affinity for both TNFR1 and TNFR2, which has made it difficult to create novel mutants with high selectivity and full bioactivity.[20] Therefore, functional analysis of TNFR using these mutants has not progressed sufficiently.

We previously developed a modified phage display technique that can be used to create desired functional mutant proteins. Using this technique, we have successfully created many mutants with high bioactivity,[21] high *in vivo* stability,[22] and antagonist activity[23] that are suitable for drug development. The advantage of this method is that it allows us to obtain information about specific functions and associated sequences, which is very useful for determining the structure–function relationship of a specific protein. This information will be useful for improving the design of therapeutic mutants.

In the present study, we used the phage display technique to create novel receptor-selective TNF mutants with full bioactivity. Structural information of the mutants was determined by crystallographic analysis, and structural simulation was used to determine a feasible basis for receptor selectivity. These TNF mutants will be useful tools for analyzing TNFR signaling. An understanding of the structure and sequence of these functional mutants, combined with bioinformatics techniques, can potentially lead to the design of a desired functional protein, peptide, or peptide mimic, and thus accelerate the development of novel strategies for analyzing disease-related proteins, such as TNF, and the development of associated therapies.

Results

Library construction and selection of receptor-selective TNF mutants

To create receptor-specific TNF mutants using our phage display system, we prepared two phage libraries, Libraries I and II. Each library contained six amino acids randomized in a receptor binding site suggested by point mutation analysis and X-ray crystallography (Fig. 1).[16,17,24] For construction of the TNF mutant library, a mutant TNF-Lys(−) gene was used as template for polymerase chain reaction (PCR) mutagenesis.[22] Sequence analysis of randomly selected clones indicated that Libraries I and II contained 8.2×10^6 and 5.6×10^6 independent clones, respectively. For selection from the library, several rounds of affinity panning were performed against human TNFR1 or TNFR2 using BIAcore 3000. Potent binders to TNFR1 or TNFR2 were concentrated in the library through this panning procedure. The monoclonal candidates in each library were picked up for enzyme-linked immunosorbent assay (ELISA) screening to confirm their receptor binding specifi-

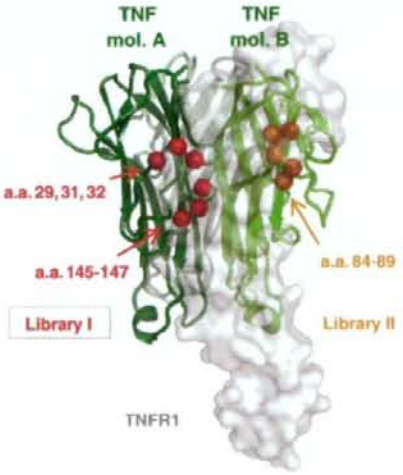

Fig. 1. Positions of randomized residues on the binding interface of the TNF–TNFR1 complex. Mutational residues of Library I (red spheres) and Library II (orange spheres). Green cartoon represents wtTNF. White area represents the surface of the TNFR1 monomer. This binding model structure of the TNF–TNFR1 complex was constructed based on the crystal structure of the LTα–TNFR1 complex (1TNR) and that of wtTNF (1TNF).

Table 1. Substituted residues of TNF mutants from Libraries I and II

			29	31	32	84	85	86	87	88	89	145	146	147
		wtTNF	L	R	R	A	V	S	Y	Q	T	A	E	S
		mutTNF-Lys(−)	—	—	—	—	—	—	—	—	—	—	—	—
TNFR1-selective candidates	Library I (29:32–145:147)	R1-1	I	—	—	—	—	—	—	—	—	—	—	—
		R1-2	Q	—	W	—	—	—	—	—	—	—	—	—
		R1-3	T	G	Y	—	—	—	—	—	—	—	—	—
		R1-4	T	K	Y	—	—	—	—	—	—	—	—	—
		R1-5	T	—	F	—	—	—	—	—	—	—	T	—
		R1-6	K	A	G	—	—	—	—	—	—	—	S	T
	Library II (84:89)	R1-7	—	—	—	S	K	T	—	T	H	—	—	—
		R1-8	—	—	—	S	P	L	—	P	K	—	—	—
		R1-9	—	—	—	S	T	N	—	N	G	—	—	—
		R1-10	—	—	—	T	S	A	—	G	P	—	—	—
		R1-11	—	—	—	T	T	A	—	S	G	—	—	—
		R1-12	—	—	—	T	H	K	—	P	Q	—	—	—
		R1-13	—	—	—	S	K	T	—	S	H	—	—	—
		R1-14	—	—	—	S	S	H	—	R	F	—	—	—
TNFR2-selective candidates	Library I (29:32–145:147)	R2-1	—	—	—	—	—	—	—	—	—	K	D	T
		R2-2	—	—	—	—	—	—	—	—	—	R	T	D
		R2-3	—	—	—	—	—	—	—	—	—	R	E	T
		R2-4	—	—	—	—	—	—	—	—	—	A	D	D
		R2-5	—	—	—	—	—	—	—	—	—	A	N	D

Conserved residues compared with wtTNF are indicated by an em dash (—). Mutated residues in each library are highlighted in gray. Library I included mutated residues 29, 31, 32, and 145–147. Library II contained mutated residues 84–89. R1-1–R1-6 and R1-7–R1-14 were isolated from Libraries I and II, respectively, as TNFR1-selective candidates. TNFR2-selective clones R2-1–R2-5 were isolated from Library I; Library II contained no TNFR2-selective clones.

city. Several clones with TNFR1 or TNFR2 specificity were eventually obtained.

Sequence analysis of receptor-specific TNF mutant candidates

Sequence analysis revealed that we had 14 TNFR1-selective candidates (R1-1–R1-14) and 5 TNFR2-selective candidates (R2-1–R2-5) from Libraries I and II (Table 1). Unfortunately, Library II did not contain any TNFR2-selective mutants. All active TNFR1-selective mutants in Library II retained Tyr87, suggesting that Tyr87 was an essential residue for receptor binding. Analysis of Library I, however, revealed that the mutated and conserved regions of the TNFR1-selective mutants were different from

Table 2. Receptor-selective bioactivities and affinities of TNF mutants

			Relative affinity (% K_d)[a]			Relative bioactivity (% of EC_{50})		
		TNFs	TNFR1	TNFR2	R_1/R_2	HEp2[b]	PC60[c]	R_1/R_2
		wtTNF	100	100	1.0	100	100	1.0
		mutTNF-Lys(−)	108	88	1.2	116	126	0.9
TNFR1-selective candidates	Library I (29:32–145:147)	R1-1	145	121	1.2	492	NT	—
		R1-2	212	32	6.7	436	NT	—
		R1-3	42	18	2.4	343	NT	—
		R1-4	43	3	13.4	447	NT	—
		R1-5	177	2	106.2	582	36	16.2
		R1-6	33	4	8.4	128	<0.07	>1800.0
	Library II (84:89)	R1-7	108	13	8.4	102	NT	—
		R1-8	145	9	16.5	120	173	0.7
		R1-9	175	24	7.4	110	NT	—
		R1-10	149	9	17.0	134	NT	—
		R1-11	219	11	20.4	58	NT	—
		R1-12	51	15	3.5	21	NT	—
		R1-13	51	11	4.6	26	NT	—
		R1-14	46	4	12.0	47	47	1.0
TNFR2-selective candidates	Library I (29:32–145:147)	R2-1	83	112	0.741	12.4	23	0.539
		R2-2	3	143	0.020	0.2	30	0.007
		R2-3	38	225	0.169	2.5	12	0.208
		R2-4	51	572	0.089	6.2	19	0.326
		R2-5	94	324	0.290	13.4	39	0.344

The affinity and bioactivity values are shown as relative values (% wtTNF).

NT, not tested.

[a] Affinity for immobilized TNFR1 and TNFR2 was assessed by SPR using BIAcore 3000.

[b] Human TNFR1-mediated bioactivity was evaluated using a HEp-2 cell cytotoxicity assay. In this assay, HEp-2 cell viability was determined by methylene blue staining. Each value represents the mean±SD.

[c] Human TNFR2-mediated bioactivity was evaluated using PC60-R2 assay. GM-CSF expression by TNFR2-mediated signaling was detected by ELISA. Each value presents the mean±SD.

those of the TNFR2-selective mutants. TNFR1-selective mutants were highly mutated near residue 30 and conserved near residue 140. On the other hand, TNFR2-selective mutants were mutated near residue 140 and conserved near residue 30. This interesting result suggested that the details of the essential binding interface for TNFR1 and TNFR2 differed despite their predicted similar complex forms.[19]

Receptor selectivity and bioactivity of TNF mutants

To investigate the properties of candidate receptor-selective TNF mutants in detail, we prepared recombinant protein using the previously described methods.[21,22] TNF mutants expressed as an inclusion body in *Escherichia coli* were denatured and refolded. Then, active TNF mutants were purified by ion-exchange and gel-filtration chromatography. TNF mutant purity was greater than 90% in sodium dodecyl sulfate–polyacrylamide gel electrophoresis, and all mutants were confirmed to form trimers by gel-filtration analysis (data not shown).

We examined the affinities of these recombinant TNF mutants for TNFR1 and TNFR2 (Table 2). Most of the TNFR1-selective candidates had little affinity for TNFR2 based on surface plasmon resonance (SPR) analysis by BIAcore 3000. In particular, the TNFR1 affinities of R1-2, R1-5, R1-8, R1-9, R1-10, and R1-11 were higher than that of wild-type TNF (wtTNF), despite the loss of their TNFR2 affinities. TNFR1- and TNFR2-mediated bioactivities were assessed by HEp-2 and PC60-hTNFR2 assays, respectively. Interestingly, R1-selective candidates from Library I showed more potent activity via TNFR1 than those from Library II. R1-5 and R1-6 showed superior bioactivity and receptor selectivity. R1-6 was selected as the best overall mutant with greater than 1800-fold selective TNFR1 activity. These mutants were novel because TNFR1-selective mutants with higher bioactivity had not yet been established. Similar studies were performed with the TNFR2-selective candidates. In SPR analysis, these candidates showed higher TNFR2 affinity than wtTNF. Unfortunately, however, none of the TNFR2-selective candidates could sufficiently activate TNFR2 and had less than 40% of the bioactivity of wtTNF.

Next, we performed a competitive binding assay to confirm the details of the TNFR1 selectivity of R1-5 and R1-6—the candidates with the highest selectivity for TNFR1. Competitive affinities were assessed under a certain amount of wtTNF-FLAG, wtTNF fusing FLAG-tag (DYKDDDDK) at C-terminal, as competitor (Fig. 2). Similar to the results of the SPR analysis, R1-5 showed a higher affinity for TNFR1 compared with wild type, and its affinity for TNFR2 was decreased to approximately 10% that for wtTNF, suggesting that R1-5 was a TNFR1-selective mutant. In contrast to the SPR results, however, R1-6 showed a higher competitive affinity for TNFR1, and wtTNF–FLAG binding to TNFR2 was not completely inhibited, even by excess R1-6, which suggested that R1-6

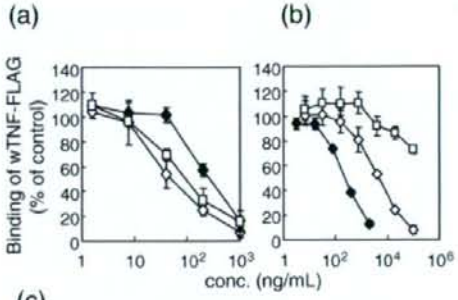

(c)

	TNFR1		TNFR2	
	IC50 (ng/ml)	(%)	IC50 (ngml)	(%)
wtTNF	276.0	100.0	508.1	100.0
R1-5	57.7	478.3	4606.6	11.0
R1-6	105.4	261.9	> 100000.0	< 0.5

Fig. 2. Competitive binding affinities of TNFR1-selective mutants (R1-5 and R1-6). Competitive affinities were assessed under 50 ng/ml FLAG-tagged wtTNF (wtTNF–FLAG) as competitor. Both (a) TNFR1 and (b) TNFR2 were immobilized. Binding of wtTNF–FLAG was inhibited by serially diluted TNF mutants. Final binding of wtTNF–FLAG was assessed by ELISA. Each value represents the mean±SD. (c) IC_{50} values are given as the concentration of the TNF mutant required to inhibit 50% of the maximal binding of wtTNF–FLAG.

lacked binding potency to TNFR2. Because the TNF binding interfaces to the receptors are known to overlap,[19] TNFR1 selectivity caused by a structural change in the R1-6 surface might provide important information for structure-based drug discovery.

X-ray crystallography of TNFR1-selective TNF mutant R1-6

The structural basis of the TNFR1 selectivity of R1-6 was examined by X-ray crystallography. After establishing crystallization conditions, good-quality crystals of R1-6 were obtained (approximately 0.2 mm × 0.2 mm × 0.3 mm in size). X-ray diffraction data were collected in SPring-8 (a large synchrotron radiation facility in Harima, Japan). Analysis of these data indicated that the space group is *R*3 and that the lattice constants are $a = 135.87$ Å, $b = 135.87$ Å, and $c = 58.02$ Å (Table 3). The R1-6 structure was further refined using the CNS software suite. The results of model validation using the PROCHECK program indicated that there were 86.9% residues in the most favored regions, 13.1% residues in the additionally allowed regions, 0.0% residues in the generously allowed regions, and 0.0% residues in the disallowed regions.

The overall structures of the R1-6 [Protein Data Bank (PDB) code 2ZJC] and wtTNF (PDB code 1TNF) trimers are also similar and superimpose with an rmsd of 1.21 Å for 428 C^{α} atoms (Fig. 3). The structure of

Table 3. Crystallographic parameters and refinement statistics of the R1-6 crystal

Data collection	
Resolution (Å)	50–2.50 (2.59–2.50)
Cell constants (Å)[a]	135.9, 135.9, 58.0
Space group	*R*3
Measured reflections	74,516
Unique reflections	13,445 (1173)
Completeness (%)	99.9 (85.2)
R_{merge} (%)[b]	0.10 (0.53)
$I/\sigma(I)$	28.9 (4.2)
Refinement statistics	
Resolution (Å)	25.67–2.50
Reflections used	12,060
R_{cryst} (%)[c]	20.1
R_{free} (%)[d]	27.2
Completeness (%)	97.1
Atoms	
Protein; water	3338; 59
rmsd from ideality	
Bond lengths (Å); bond angles (°)	0.009; 1.27
Overall *B*-factor (Å^2)	19.7
B-factor rmsd (Å^2)	
Main-chain bonds; side-chain bonds	0.42; 0.77
Main-chain angles; side-chain angles	0.94; 1.48
Ramachandran plot statistics	
Most favored regions (%)	86.9
Additionally allowed regions (%)	13.1
Generously allowed regions (%)	0.0
Disallowed regions (%)	0.0

Values in parentheses are those for the outer shell.

[a] Cell constants are *a*, *b*, and *c*.

[b] $R_{merge} = \sum |I - \langle I \rangle| / \sum \langle I \rangle$, where I is intensity of the observations. R_{merge} in the last shell is high because of the anisotropic mosaicity of the crystal.

[c] $R_{cryst} = \sum ||F_o| - |F_c|| / \sum |F_o|$, where F_o and F_c are the observed and calculated structure factors, respectively.

[d] R_{free} is calculated as for R_{cryst} but for the test set comprising reflections not used in refinement. The overall *B*-factor was calculated after TLS parameter analysis (TLSANL) using Refmac.

each monomer is similar to each other (rmsd of 0.98–1.12 Å for 140 C^α atoms). Especially, the structures of the β-sheet in each monomer are essentially the same (rmsd of 0.31–0.42 Å for 63 C^α atoms). These features have been found in the wtTNF trimer.[25]

The R1-6 loop structure near mutational residues 31 and 32 is different from that in wtTNF (Fig. 4). This loop structure between monomers is not different (wtTNF: rmsd of 0.61–0.72 Å for 11 C^α atoms; R1-6: rmsd of 0.39–0.91 Å for 11 C^α atoms) (Fig. 4a and b). However, they are clearly different between wtTNF and R1-6 (Fig. 4c). This structural change is thought to be caused by R32G mutation from a sterically bulky arginine residue to a flexible glycine residue. Because this region is close to the TNFR surface, such a structural change in the C^α chain could influence receptor binding. Additional TNF–TNFR docking simulation studies are discussed below.

Discussion

We recently developed the technology to create functional mutant proteins with high bioactivity, high *in vivo* stability, and antagonistic activity.[21–23] Here, we attempted to establish fully bioactive receptor-selective TNF mutants for functional analysis of TNFR1 and TNFR2 using our optimized phage display system. We constructed TNF mutant libraries (Libraries I and II) in which six residues near the receptor binding region were randomized (Fig. 1). From these libraries, we screened for TNFR1- or TNFR2-selective binders, and isolated receptor-selective candidates (Table 1). Despite the successful isolation of TNFR2-selective binders, the TNFR2-selective candidates obtained could not sufficiently activate TNFR2. This result suggested that the production of TNFR2-selective mutants was very rare in our library and that an improved panning method was necessary.

One advantage of our phage-display-based technique is that it can be used to obtain the sequence information of many mutants (Table 1). Tyr87 of TNF was conserved in all mutants obtained from Library II. This residue is highly conserved throughout the TNF superfamily, such as in LTα, LTβ, and LIGHT, and site-directed mutagenesis of the Tyr87 residue of TNF results in a dramatic loss of its biologic activity and its affinities for both TNFR1 and TNFR2.[17] In addition, Tyr87 replacement in antagonistic TNF causes unstable receptor binding and loss of receptor activation in our report.[23] These findings together indicate that Tyr87 is an essential residue for receptor signaling and receptor complex stability.

TNFR1-selective mutants had mutations near residue 30 and conserved residues near residue 140. In contrast, TNFR2-selective mutants had mutations near residue 140 and conserved residues near residue 30. These findings support those of previous point mutation analyses[15–17] and suggest that our phage-

Fig. 3. Overall structure of wtTNF and R1-6. Merge image of previously reported wtTNF structure (green; 1TNF) and refined structure of R1-6 (white; 2ZJC). The flexible loop containing residues 100–110 shown at the bottom of the figure was disordered in the R1-6 structure.

Fig. 4. Structural difference in receptor binding loop between wtTNF and R1-6. Each TNF monomer was superimposed using the CCP4i program. Details of the receptor binding loop, including residues 31 and 32, are shown in these figures. (a) Loops of wtTNF monomers (green); (b) loops of R1-6 monomers (white); (c) merged image of the loops of wtTNF and R1-6; (d) $2F_o - F_c$ map contoured at 1.0σ of R1-6 loop (pink mesh). The different C^α chains are highlighted by the dashed orange circle in (c).

display-based technique can be used to rapidly gather important information about the function–sequence relationships determined by long-term point mutation analysis. In the present study, we successfully isolated mutants that retained TNFR affinity from a huge phage library containing over a million repertoires. Most of the mutants in the library had no TNFR affinity and were therefore discarded through this selection step. This finding may indicate that the mutational residues in these unbound clones diminish TNFR affinity. This method may be useful for examining the function, capability, and sequence–function relationship of unknown cytokines and proteins.

Using these receptor-selective candidates, we expressed recombinant proteins and estimated their bioactivities and affinities for TNFR1 and TNFR2. R1-6, the most highly TNFR1-selective mutant, bound and activated TNFR1 efficiently despite the loss of its affinity for TNFR2. X-ray crystallography of R1-6 revealed that the crystal structure of R1-6 was a trimer (similar to wtTNF), and no other salient differences in the overall structure were observed. Superimposition of wtTNF and R1-6 sequences, however, revealed that the C^α of the receptor binding loop near residue 30 was partially different (Fig. 4). This change might influence the receptor binding mode of R1-6. We further used the superimposition program to perform docking simulations with TNF and TNFR1 based on the crystal structure of the LTα–TNFR1 complex (PDB code 1TNR).[18]

Based on the model wtTNF–TNFR1 complex, Arg31 of TNF would interact electrostatically with Glu56 of TNFR1. The main chain of TNF was too close to His69 of TNFR1, however, potentially causing potential steric hindrance (Fig. 5a). On the other hand, a structural change in the loop in R1-6, however, was thought to solve this problem (Fig. 5b). Arg32 of wtTNF associated with Ser72 of TNFR1 (Fig. 5a). In the R1-6 structure, however, this role of Arg32 was thought to be compensated for by Lys29 (Fig. 5b). This speculation was supported by the crystal structure of the LTα–TNFR1 complex.[18] The position of Lys29 in R1-6 corresponded to that of Arg46 in LTα interacting with Ser72 of TNFR1 by hydrogen bonding. This interesting "compensating role of an amino acid" would be difficult to induce using single point mutation methods, which is another advantage of our modified phage display technique.

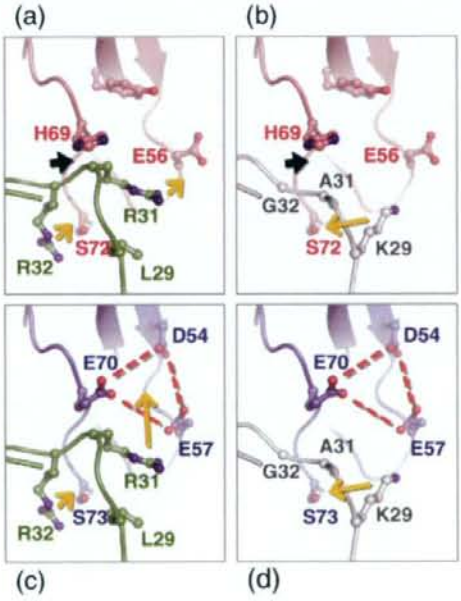

Fig. 5. Model of TNF binding to TNFR1 and TNFR2. Receptor binding interfaces of (a) wtTNF–TNFR1 (green–red); (b) R1-6–TNFR1 (white–red); (c) wtTNF–TNFR2 (green–blue); and (d) R1-6–TNFR2 (white–blue). The TNF–TNFR1 model complex was constructed from 1TNF (wtTNF) and 1TNR (LTα–TNFR1 complex). The predicted TNFR2 structure was constructed by side-chain mutation using the O program. In this simulation, the side chains of each structure were rotated to fit the predicted interaction. Stable structures of these rotamers were constructed using the O program. Steric hindrance might have occurred between His69 of TNFR1 and Arg32 of wtTNF in (a) (black arrowhead). Potential interactions are indicated by orange arrows. A cluster of anionic charged residues (Asp54, Glu57, and Glu70) is highlighted by a broken red line.

Next, we examined the TNFR1 selectivity of R1-6 based on its structure. Because the structure of TNFR2 is thought to be similar to that of TNFR1,[18] we generated a model structure of TNFR2 by manual mutation based on the crystal structure of TNFR1. This TNF–TNFR2 simulation is speculative, but this model, together with the information obtained from previous mutation studies, can be used to form hypotheses regarding the important structural features for TNFR1 selectivity. The binding surface of TNFR2 was composed of Asp54, Glu57, and Glu70, which could cause a strongly negatively charged surface of TNFR2 different from that of TNFR1 (Fig. 5c and d). Arg31 of wtTNF was thought to have an important role in TNFR2 binding by strongly interacting with this surface (Fig. 5c). R1-6 had an R31A mutation, however, which could cause the loss of the affinity of R1-6 for TNFR2 (Fig. 5d). In support of this finding, a single point mutation R31E mutant was previously reported to have a dramatic loss of affinity for TNFR2.[12,14] On the other hand, the R32W mutant is also reported to be a mutant with TNFR1 selectivity.[12] From our library, Arg32 of our TNFR1-selective candidates was replaced with hydrophobic or nonionic amino acids (Trp, Tyr, Phe, and Gly), which might indicate the importance of Arg32 for binding to TNFR2 (Table 1). This structural information, in combination with bioinformatics technology, will be useful for designing more advanced TNFR-selective mutants and TNFR-selective inhibitors (peptide mimics and chemical compounds).

In conclusion, the phage display technique is an attractive method for creating functional mutants, as demonstrated here by the production of TNFR-specific mutants. Application of this method to various cytokines and proteins will enhance the construction of useful receptor-selective mutants and accelerate functional analysis of these proteins. As an advanced application, analysis of the "structure (sequence)–function relationship" using the obtained mutants will be a powerful technique for basic life science research and drug discovery.

Materials and Methods

Cell culture

HEp-2 cells (a human fibroblast cell line) were provided by the Cell Resource Center for Biomedical Research (Tohoku University) and maintained with RPMI 1640 containing 10% fetal bovine serum and antibiotics. PC60-hTNFR2 cells (a mouse–rat fusion hybridoma comprised of human TNFR2-transfected PC60 cells) were provided by Dr. Vandenabeele and maintained in RPMI 1640 supplemented with 10% fetal bovine serum, 1 mM sodium pyruvate, 5×10^{-5} M 2-mercaptoethanol, 3 μg/ml puromycin, and antibiotics (100 U/ml penicillin, 100 μg/ml streptomycin, and 0.25 μg/ml amphotericin B).

Library construction

The pCANTAB phagemid vector (GE Healthcare Ltd., UK) encoding mutTNF-Lys(−) was used as template for PCR. This TNF was previously reported to be a fully active lysine-deficient TNF mutant.[22] Mutations were introduced in TNF at six amino acid codons (Library I: amino acid residues 29, 31, 32, and 145–147; Library II: amino acid residues 84–89) using a two-step PCR. Three primers, Oligos A, B, and C, were used for the construction of Library I. The first PCR was performed using Oligos A and B. The PCR conditions were 5 min at 95 °C, 35 cycles of denaturization at 95 °C for 15 s, and annealing/extension at 68 °C for 2 min. This first PCR product and Oligo C were then annealed to the template, and PCR was performed again under the same conditions. For the construction of Library II, Oligos A, D, and E were used. The first PCR was performed using Oligos A and D. The first PCR product and Oligo E were used as primers for the second PCR. The PCR conditions of Library II were the same as those of Library I. After the second PCR, the PCR products were digested with HindIII and NotI, and then ligated to a pY03′ phagemid vector (modified from pCANTAB) for the display of TNF variants on the phage surface as g3p fusion proteins. The primer sequences used in this experiment are listed below. Oligos A and E were designed to prime to the pCANTAB vector sequence: Oligo A: 5′-GATAACAATTTCACACAGGAAACAGCTATGACCATGATTACGCCAAGCTTTGGAGCC-3′; Oligo B: 5′-CGCCATTGGCCAGGAGGGCATTAGCSNNSNNGTTSNNCCACTGGAGCTGCCCCTCAGCTTGAGGG-3′; Oligo C: 5′-CCAGCGGATCCGGATACGGCACCGGCGCACCTGCGGCCGCGGATCCACCACCACCCAGGGCAATGATCCCAAAGTAGACCTGCCCSNNSNNSNNAAAGTCGAGATAGTCGGGCCGATTGA-3′; Oligo D: 5′-CTGGCAGGGGCTGCGGATGGCAGAGAGGAGATTGACGGGSNNSNNSNNSNNSNNGATGCGGCTGATGGTGTGGGTGAGGAGCAC-3′; Oligo E: 5′-TGCGGCACGCGGTTCCAGCGGATC-3′.

Isolation of receptor-selective TNF mutants from the library (affinity panning and screening)

Human TNFR1 Fc (R&D Systems, Inc., Minneapolis, MN) and TNFR2 Fc (R&D Systems, Inc.) were diluted to 50 μg/ml in 10 mM sodium acetate buffer (pH 4.5) and immobilized on a CM3 sensor chip using an amine coupling kit (GE Healthcare Ltd.), which resulted in an increase of 4000–6000 resonance units. The phage library (1×10^{11} colony-forming units/100 μl) was injected at 3 μl/min over the sensor chip. After binding and until the association phase had been reached, the sensor chip was washed using the rinse command and eluted using 20 μl of 10 mM glycine–HCl. The eluted phage was neutralized with 1 M Tris–HCl (pH 6.9). *E. coli* (TG1) was infected with the collected phage for amplification. This panning cycle was performed two more times. After picking up a single clone of transfected *E. coli*, the phagemid vectors were sequenced using a Big Dye Terminator v3.1 kit and ABI PRISM 3100 (Applied Biosystems Ltd., Pleasanton, CA). After the procedure, the binding affinities of the TNF mutants were assessed by ELISA, and their bioactivities through TNFR1 were determined by cytotoxicity assay in human HEp-2 cells.

Expression and purification of TNF mutants

The protocol for the expression and purification of recombinant protein was the same as that described previously.[21,22] Briefly, TNF mutants were produced in the *E. coli* BL21(DE3) strain. The inclusion body of each

TNF mutant was washed in 2.5% Triton X-100 and solubilized in 6 M guanidine–HCl, 0.1 M Tris–HCl (pH 8.0), and 2 mM ethylenediaminetetraacetic acid. Solubilized protein at 10 mg/ml was reduced with 10 mg/ml dithioerythritol for 4 h at room temperature and refolded by 100-fold dilution in a refolding buffer (100 mM Tris–HCl, 2 mM ethylenediaminetetraacetic acid, 0.5 M arginine, and 551 mg/L oxidized glutathione). After dialysis with 20 mM Tris–HCl (pH 7.4) containing 100 mM urea, active trimeric proteins were purified by ion-exchange chromatography using Q-Sepharose FF (GE Healthcare Ltd.). Size-exclusion chromatography was performed using a Superose 12 column (GE Healthcare Ltd.).

In vitro bioactivity of TNF mutants

HEp-2 cells were used for cytotoxicity assay in the presence of cycloheximide (50 μg/ml). HEp-2 cytotoxicity was dependent on TNFR1 signaling. HEp-2 cells were cultured in 96-well plates in the presence of TNF mutants and serially diluted mouse or human wtTNF (PeproTech EC Ltd., UK) at 4×10^4 cells/well. For neutralization assay, cells were cultured in the presence of a constant concentration of human (20 ng/ml) wtTNF and a serial dilution of TNF mutants. After incubation for 18 h, cell survival was determined by methylene blue assay, as described previously.[21,22] To evaluate the bioactivity of the TNF mutant binding specifically to TNFR2, PC60-hTNFR2 cells were used as an index of granulocyte–macrophage colony-stimulating factor (GM-CSF) production, as described previously.[26] Briefly, PC60-hTNFR2 cells were cultured at 5×10^4 cells/well with interleukin-1β (2 ng/ml) and serially diluted TNF mutant. After 24 h of incubation, the amount of rat GM-CSF produced was quantified by ELISA in accordance with the manufacturer's protocol (R&D Systems, Inc.).

Affinity assessment using SPR

The binding kinetics of wtTNF and TNF mutants were analyzed using the BIAcore 3000 SPR system (GE Healthcare Ltd.). TNFRs were immobilized on a CM5 sensor chip, which resulted in an increase of 3000–5000 resonance units. During the association phase, TNF mutants or wtTNF diluted in HBS-EP running buffer (10 mM HEPES pH7.4, 150 mM NaCl, 3 mM EDTA, 0.005% Tween20, GE Healthcare Ltd.) at 78.4, 26.1, or 8.7 nM were individually passed over the immobilized TNFR at a flow rate of 20 μl/min. During the dissociation phase, HBS-EP buffer was applied to the sensor chip at a flow rate of 20 μl/min. The data were analyzed globally with BIAEVALUATION 3.0 software (GE Healthcare Ltd.) using a 1:1 binding model.

Competitive binding of TNF to TNFR1 and TNFR2 (ELISA)

Goat anti-human IgG (MP Biomedicals, Inc., Solon, OH) was immobilized on Maxisorb 96-well ELISA plates (Nalge Nunc International KK, Japan), and nonspecific binding to the plates was blocked using Block Ace (Dainippon Sumitomo Pharma Co., Ltd., Japan). Human TNFR1-Fc or human TNFR2-Fc (ALEXIS Corporation, Switzerland) was bound to coated antibody. Serially diluted TNF with 50 ng/ml FLAG-tagged wtTNF (wtTNF–FLAG) was added to TNFR1-Fc or TNFR2-Fc in 0.4% Block Ace. wtTNF–FLAG binding was detected by anti-FLAG M2 antibody (Sigma-Aldrich Corporation, St. Louis, MO) and avidin horseradish peroxidase conjugate (Invitrogen Corporation, Carlsbad, CA). The binding affinity of TNF was assessed by competitive wtTNF–FLAG binding to TNFR (IC_{50} value).

X-ray crystallography

Purified R1-6 was concentrated to 10 mg/ml in 20 mM Tris–HCl (pH 7.4). Initial screening using a Hampton Crystal screen 1-2 and Crystal screen Lite kit (Hampton Research Corporation, Aliso Viejo, CA) was performed by vapor diffusion method with hanging drops (1+1 μl) at 20 °C. After optimization of the crystallization conditions, rhombohedral crystals (0.2 mm × 0.2 mm × 0.3 mm) were obtained with reservoir solution containing 0.5 M ammonium sulfate, 1.2 M lithium sulfate, and 0.1 M trisodium citrate (pH 5.6). The crystals were frozen in a cryopreserving solution containing 15% glycerol as cryoprotectant. X-ray diffraction data to 2.5 Å resolution were collected at BL41XU, SPring-8, under flash cooling to 100 K to reduce the effects of radiation damage. Data integration and scaling were performed using HKL2000.[27] Molecular replacement was performed by the MOLREP program in CCP4i[28] using a crystal structure of the wtTNF (1TNF)[25] as search model. Cycles of manual rebuilding using the O program[29] and refinement using the CNS program[30] led to a refined structure. Final refinement (TLS refinement) was performed using the Refmac program in CCP4i.[28] Final model validation was performed using PROCHECK program in CCP4i.[28] The model complexes of TNF–TNFR1 and R1-6–TNFR1 were constructed based on the crystal structure of the LTα–TNFR1 complex[18] using the superimposing program in CCP4i. Structural models of TNFR2 were constructed based on the TNFR1 structure by manual mutation using the O program.[29]

Accession number

Coordinates and structure factors have been deposited in the PDB with accession number 2ZJC.

Acknowledgements

This study was supported by Research for Promoting Technological Seeds (no. 11-067) from the Japan Science and Technology Agency; Research Fund Project on Health Sciences focusing on Drug Innovation (no. KAA3701) from the Japan Health Sciences Foundation; the Global COE Program *"In Silico* Medicine" (Wakate-16) at Osaka University; a Grant-in-Aid for Young Scientists (B) (no. 20790134) and Grants-in-Aid for Scientific Research (nos. 18015055 and 17689008) from the Ministry of Education, Culture, Sports, Science, and Technology of Japan; and Research Fellowships for Young Scientists (no. 20-3919) from the Japan Society for the Promotion of Science.

References

1. Aggarwal, B. B. (2003). Signalling pathways of the TNF superfamily: a double-edged sword. *Nat. Rev. Immunol.* **3**, 745–756.

2. Feldmann, M. & Maini, R. N. (2003). Lasker Clinical Medical Research Award. TNF defined as a therapeutic target for rheumatoid arthritis and other autoimmune diseases. *Nat. Med.* **9**, 1245–1250.
3. Kooloos, W. M., de Jong, D. J., Huizinga, T. W. & Guchelaar, H. J. (2007). Potential role of pharmacogenetics in anti-TNF treatment of rheumatoid arthritis and Crohn's disease. *Drug Discov. Today*, **12**, 125–131.
4. Rutgeerts, P., Van Assche, G. & Vermeire, S. (2004). Optimizing anti-TNF treatment in inflammatory bowel disease. *Gastroenterology*, **126**, 1593–1610.
5. Rothe, J., Lesslauer, W., Lötscher, H., Lang, Y., Koebel, P., Köntgen, F. *et al.* (1993). Mice lacking the tumour necrosis factor receptor 1 are resistant to TNF-mediated toxicity but highly susceptible to infection by *Listeria monocytogenes*. *Nature*, **364**, 798–802.
6. Kafrouni, M. I., Brown, G. R. & Thiele, D. L. (2003). The role of TNF–TNFR2 interactions in generation of CTL responses and clearance of hepatic adenovirus infection. *J. Leukocyte Biol.* **74**, 564–571.
7. Rahman, M. M. & McFadden, G. (2006). Modulation of tumor necrosis factor by microbial pathogens. *PLoS Pathog.* **2**, e4.
8. Chan, F. K., Shisler, J., Bixby, J. G., Felices, M., Zheng, L., Appel, M. *et al.* (2003). A role for tumor necrosis factor receptor-2 and receptor-interacting protein in programmed necrosis and antiviral responses. *J. Biol. Chem.* **278**, 51613–51621.
9. Wajant, H., Pfizenmaier, K. & Scheurich, P. (2003). Tumor necrosis factor signaling. *Cell Death Differ.* **10**, 45–65.
10. Weiss, T., Grell, M., Siemienski, K., Mühlenbeck, F., Dürkop, H., Pfizenmaier, K. *et al.* (1998). TNFR80-dependent enhancement of TNFR60-induced cell death is mediated by TNFR-associated factor 2 and is specific for TNFR60. *J. Immunol.* **161**, 3136–3142.
11. Fotin-Mleczek, M., Henkler, F., Samel, D., Reichwein, M., Hausser, A., Parmryd, I. *et al.* (2002). Apoptotic crosstalk of TNF receptors: TNF-R2-induces depletion of TRAF2 and IAP proteins and accelerates TNF-R1-dependent activation of caspase-8. *J. Cell Sci.* **115**, 2757–2770.
12. Van Ostade, X., Vandenabeele, P., Everaerdt, B., Loetscher, H., Gentz, R., Brockhaus, M. *et al.* (1993). Human TNF mutants with selective activity on the p55 receptor. *Nature*, **361**, 266–269.
13. Barbara, J. A., Smith, W. B., Gamble, J. R., Van Ostade, X., Vandenabeele, P., Tavernier, J. *et al.* (1994). Dissociation of TNF-alpha cytotoxic and pro-inflammatory activities by p55 receptor- and p75 receptor-selective TNF-alpha mutants. *EMBO J.* **13**, 843–850.
14. Van Ostade, X., Vandenabeele, P., Tavernier, J. & Fiers, W. (1994). Human tumor necrosis factor mutants with preferential binding to and activity on either the R55 or R75 receptor. *Eur. J. Biochem.* **220**, 771–779.
15. Van Ostade, X., Tavernier, J. & Fiers, W. (1994). Structure–activity studies of human tumour necrosis factors. *Protein Eng.* **7**, 5–22.
16. Yamagishi, J., Kawashima, H., Matsuo, N., Ohue, M., Yamayoshi, M., Fukui, T. *et al.* (1990). Mutational analysis of structure–activity relationships in human tumor necrosis factor-alpha. *Protein Eng.* **3**, 713–719.
17. Zhang, X. M., Weber, I. & Chen, M. J. (1992). Site-directed mutational analysis of human tumor necrosis factor-alpha receptor binding site and structure–functional relationship. *J. Biol. Chem.* **267**, 24069–24075.
18. Banner, D. W., D'Arcy, A., Janes, W., Gentz, R., Schoenfeld, H. J., Broger, C. *et al.* (1993). Crystal structure of the soluble human 55 kD TNF receptor-human TNF beta complex: implications for TNF receptor activation. *Cell*, **73**, 431–445.
19. Fu, Z. Q., Harrison, R. W., Reed, C., Wu, J., Xue, Y. N., Chen, M. J. & Weber, I. T. (1995). Model complexes of tumor necrosis factor-alpha with receptors R1 and R2. *Protein Eng.* **8**, 1233–1241.
20. Reed, C., Fu, Z. Q., Wu, J., Xue, Y. N., Harrison, R. W., Chen, M. J. & Weber, I. T. (1997). Crystal structure of TNF-alpha mutant R31D with greater affinity for receptor R1 compared with R2. *Protein Eng.* **10**, 1101–1107.
21. Shibata, H., Yoshioka, Y., Ikemizu, S., Kobayashi, K., Yamamoto, Y., Mukai, Y. *et al.* (2004). Functionalization of tumor necrosis factor-alpha using phage display technique and PEGylation improves its anti-tumor therapeutic window. *Clin. Cancer Res.* **10**, 8293–8300.
22. Yamamoto, Y., Tsutsumi, Y., Yoshioka, Y., Nishibata, T., Kobayashi, K., Okamoto, T. *et al.* (2003). Site-specific PEGylation of a lysine-deficient TNF-alpha with full bioactivity. *Nat. Biotechnol.* **21**, 546–552.
23. Shibata, H., Yoshioka, Y., Ohkawa, A., Minowa, K., Mukai, Y., Abe, Y. *et al.* (2008). Creation and X-ray structure analysis of the tumor necrosis factor receptor-1-selective mutant of a tumor necrosis factor-alpha antagonist. *J. Biol. Chem.* **283**, 998–1007.
24. Loetscher, H., Stueber, D., Banner, D., Mackay, F. & Lesslauer, W. (1993). Human tumor necrosis factor alpha (TNF alpha) mutants with exclusive specificity for the 55-kDa or 75-kDa TNF receptors. *J. Biol. Chem.* **268**, 26350–26357.
25. Eck, M. J. & Sprang, S. R. (1989). The structure of tumor necrosis factor-alpha at 2.6 A resolution. Implications for receptor binding. *J. Biol. Chem.* **264**, 17595–17605.
26. Abe, Y., Yoshikawa, T., Kamada, H., Shibata, H., Nomura, T., Minowa, K. *et al.* (2008). Simple and highly sensitive assay system for TNFR2-mediated soluble- and transmembrane-TNF activity. *J. Immunol. Methods*, **335**, 71–78.
27. Otwinowski, Z. & Minor, W. (1997). Processing of X-ray diffraction data collected in oscillation mode. *Methods Enzymol.* **276**, 307–326.
28. Potterton, E., Briggs, P., Turkenburg, M. & Dodson, E. (2003). A graphical user interface to the CCP4 program suite. *Acta Crystallogr. Sect. D*, **59**, 1131–1137.
29. Jones, T. A., Zou, J. Y., Cowan, S. W. & Kjeldgaard, M. (1991). Improved methods for building protein models in electron density maps and the location of errors in these models. *Acta Crystallogr. Sect. A*, **47** (Pt 2), 110–119.
30. Brunger, A. T., Adams, P. D., Clore, G. M., DeLano, W. L., Gros, P., Grosse-Kunstleve, R. W. *et al.* (1998). Crystallography and NMR system: a new software suite for macromolecular structure determination. *Acta Crystallogr. Sect. D*, **54**, 905–921.

Organizer-Like Reticular Stromal Cell Layer Common to Adult Secondary Lymphoid Organs[1]

Tomoya Katakai,[2]*‡‖ Hidenori Suto,*† Manabu Sugai,*‡ Hiroyuki Gonda,*‡ Atsushi Togawa,§ Sachiko Suematsu,¶ Yukihiko Ebisuno,‖ Koko Katagiri,‖ Tatsuo Kinashi,‖ and Akira Shimizu*†‡

Mesenchymal stromal cells are crucial components of secondary lymphoid organs (SLOs). Organogenesis of SLOs involves specialized stromal cells, designated lymphoid tissue organizer (LTo) in the embryonic anlagen; in the adult, several distinct stromal lineages construct elaborate tissue architecture and regulate lymphocyte compartmentalization. The relationship between the LTo and adult stromal cells, however, remains unclear, as does the precise number of stromal cell types that constitute mature SLOs are unclear. From mouse lymph nodes, we established a VCAM-1$^+$ICAM-1$^+$MAdCAM-1$^+$ reticular cell line that can produce CXCL13 upon LTβR stimulation and support primary B cell adhesion and migration in vitro. A similar stromal population sharing many characteristics with the LTo, designated marginal reticular cells (MRCs), was found in the outer follicular region immediately underneath the subcapsular sinus of lymph nodes. Moreover, MRCs were commonly observed at particular sites in various SLOs even in Rag2$^{-/-}$ mice, but were not found in ectopic lymphoid tissues, suggesting that MRCs are a developmentally determined element. These findings lead to a comprehensive view of the stromal composition and architecture of SLOs. *The Journal of Immunology*, 2008, 181: 6189–6200.

Various types of secondary lymphoid organs (SLOs),[3] situated at strategic sites throughout the body, play important roles in triggering adaptive immunity (1). Lymph nodes (LNs) and the spleen are connected with the lymphatic and blood vascular system, respectively, to filter and detect Ags in body fluids. Mucosal-associated lymphoid organizations such as Peyer's patches (PPs), nasal-associated lymphoid tissues (NALTs), isolated lymphoid follicles (ILFs), and cryptopatches (CPs) play crucial roles in mucosal surveillance. Although each SLO has a unique architecture closely associated with the surrounding anatomy, the various SLOs share some common features: for instance, the accumulated immune cell subsets are distributed into a regular pattern to form subcompartments (1). The most prominent feature of SLOs is the segregation of B and T lymphocytes. B cells form follicles (B zone) and occasionally develop germinal centers during antigenic stimulation, while the majority of T cells accumulate adjacent to the follicles (T zone) and survey cognate Ags presented by dendritic cells (DCs). Such tissue geometry is supported by mesenchymal stromal cells, which not only provide a foothold for immune cells' movement and interactions but also have the ability to regulate their homeostasis. The reticular network, composed of fibroblastic reticular cells (FRCs) and extracellular matrix (ECM) bundles, is the chief framework supporting the whole tissue architecture (2–4). Several findings have suggested that the reticular network acts as a system for transporting materials through a "conduit" consisting of ECM bundles wrapped with FRCs, (5, 6). Two distinct stromal cell types, residing in different compartments and producing specific chemokines, play key roles in the localization of lymphocytes: in the B zone, follicular dendritic cells (FDCs) expressing CXCL13 and in the T zone, FRCs expressing CCL19 and CCL21 (7–9).

Organogenesis of SLOs is considered to progress essentially through two sequential steps: first, the early formation of anlagen and, second, the maturation of tissue architecture by lymphocyte accumulation (1). LNs and PPs develop from embryonic anlagen in a similar way (10, 11), while postnatally constructed NALT and ILFs are formed through slightly different processes (12, 13). Organogenesis of the spleen is more complicated because it consists of distinct tissues, a lymphoid compartment (white pulp) and the red pulp (14). The initial key event in LN and PP organogenesis is the intimate interaction between hematopoietic CD45$^+$CD4$^+$ CD3$^-$ lymphoid tissue "inducer" (LTi) cells and specialized mesenchymal "organizer" (LTo) cells expressing VCAM-1, ICAM-1, and mucosal addressin cell adhesion molecule 1 (MAdCAM-1) (15–18). LTi cells express lymphotoxin (LT) $\alpha1\beta2$, which transmits signals through lymphotoxin β receptor (LTβR) on LTo cells, leading to the activation of NF-κB transcription factor complexes, not only RelA/p50 (canonical pathway) but also RelB/p52 (noncanonical pathway) via NF-κB-inducing kinase (NIK) (11, 19). In LTo cells, this cascade up-regulates VCAM-1, ICAM-1, MAdCAM-1, and homeostatic chemokines, driving a positive

*Center for Genomic Medicine, Graduate School of Medicine and †Graduate School of Biostudies, Kyoto University and ‡Translational Research Center, Kyoto University Hospital, Kyoto, Japan; §Laboratory for Stem Cell Biology, RIKEN Center for Developmental Biology, Kobe, Japan; ¶Laboratory of Immune Cell Regulation, National Institute of Biomedical Innovation, Ibaraki; and ‖Department of Molecular Genetics, Institute of Biomedical Science, Kansai Medical University, Moriguchi, Japan

Received for publication July 8, 2008. Accepted for publication September 3, 2008.

The costs of publication of this article were defrayed in part by the payment of page charges. This article must therefore be hereby marked *advertisement* in accordance with 18 U.S.C. Section 1734 solely to indicate this fact.

[1] This work was supported in part by Grants-In-Aid for Science Research on Priority Areas from the Ministry of Education, Culture, Sports, Science and Technology of Japan.

[2] Address correspondence and reprint requests to Dr. Tomoya Katakai, Department of Molecular Genetics, Institute of Biomedical Science, Kansai Medical University, Moriguchi 570-8506, Japan. E-mail address: katakait@takii.kmu.ac.jp

[3] Abbreviations used in this paper: SLO, secondary lymphoid organ; CP, cryptopatch; ECM, extracellular matrix; FAE, follicle-associated epithelium; DC, dendritic cell; FDC, follicular DC; FRC, fibroblastic reticular cell; LT, lymphotoxin; LTi/o, lymphoid tissue inducer/organizer; MRC, marginal reticular cell; NALT, nasal-associated lymphoid tissue; PP, Peyer's patch; SCS, subcapsular sinus; LN, lymph node; NIK, NF-κB-inducing kinase; ILF, isolated lymphoid follicle; TRANCE, TNF-related activation-induced cytokine; DAPI, 4,6-diamidino-2-phenylindole; PTx, pertussis toxin; MAdCAM-1, mucosal addressin cell adhesion molecule 1; FAE, follicle-associated epithelium.

feedback loop by further attracting LTi cells. Mice lacking the above signaling components exhibit various degrees of SLO deficiency and malformation (19). Generation of LTi cells from fetal liver progenitor involves Id2 and RORγt; mice deficient in these gene products show a complete loss of LTi cells and lack all LNs and PPs (20–22). TNF-related activation-induced cytokine (TRANCE), a key factor in osteoclastogenesis, participates in the proliferation and differentiation of LTi cells, particularly in the LN anlagen (23); hence, all LNs but not all PPs are absent in mice deficient in TRANCE or its receptor TRANCE-R (24, 25). Conversely, IL-7Rα expressed on LTi cells and its downstream signaling pathway are essential for the development of PPs but not LNs (16, 26). Formation of splenic white pulp does not require LTi cells, but the maturation of the tissue structure depends on LTα1β2 produced by lymphocytes and LTβR signaling (14). Therefore, despite some similarities, the developmental program and molecular requirements of each SLO are clearly different.

Even after the maturation of SLOs, continuous interplay between lymphocytes and stromal cells is likely to be required for the maintenance of tissue architecture and characteristics of adult stromal cells. Despite their importance in the spatiotemporal regulation of immune cell behavior, however, only limited information about the cytological nature of adult stromal cells has been obtained so far. It remains unknown how many different mesenchymal stromal cell types exist in particular SLOs. The relationship between embryonic LTo cells and such different types of stromal cells in adult SLOs, i.e., the postnatal fate of LTo cells, is also unclear. It is possible that LTo-like cells might still exist in the adult and play some role in the maintenance of SLOs. Since variations in stromal cells might account for the differences in both developmental program and local immune responses, it is important to clarify the common features and differences between the various SLOs.

In this study, we report the detailed characterization of a reticular stromal cell line derived from adult mouse LN, which can produce CXCL13 upon LTβR signaling. We also found a layer of unique reticular cells underneath the subcapsular sinus lining of the LNs. These specialized mesenchymal cells share many characteristics with LTo cells and are commonly observed at certain places in various types of adult SLOs. Taken together, our observations provide new insights into the development and tissue organization of SLOs.

Materials and Methods

Mice

Mice were maintained at the animal facility in the Center for Genomic Medicine (Kyoto University). *aly/aly* mice were purchased from CLEA Japan. Experimental procedures involving animals were approved by the Animal Research Committee, Graduate School of Medicine, Kyoto University and conducted according to the guidelines for animal treatment of the Institute of Laboratory Animals (Kyoto University).

Cells

BLS4 and BLS12 cells were established from peripheral LNs of BALB/c mouse as described previously (4). Cells were maintained in DMEM supplemented with 100 U/ml penicillin, 100 μg/ml streptomycin, and 10% FCS. For ECM network formation, confluent BLS12 cells grown on 8-well chamber slides (Nalgen Nunc International) were cocultured with 2×10^6 LN cells for 6 days and examined for matrix production. Stable transfectants overexpressing human NIK were made using a retrovirus vector system (4). Primary B and T cells were isolated from spleen and LNs using a MACS B or T cell isolation kit (Miltenyi Biotec).

Abs and reagents

Primary Abs used for immunohistochemistry or flow cytometry were as follows: as primary reagents, ER-TR7 (BMA), FITC-anti-B220 (RA3-6B2), anti-CR1 (8C12) (BD Pharmingen), anti-MAdCAM-1 (MECA-367; Serotec), biotin-anti-CXCL13 (BAF470), biotin-anti-VCAM-1 (BAF643), anti-LYVE-1 (AF2125), anti-LTβR (AF1008; R&D Systems), anti-VCAM-1 (MK2; Immunotech), biotin-anti-CD3ε (145-2C11), PE-anti-CD4 (GK1.5), anti-ICAM-1 (YN1/1.7.4), anti-PDGFRβ (APB5), anti-TRANCE (IK22/5; eBioscience), anti-fibronectin (H-300), anti-RelB (C-19; Santa Cruz Biotechnology), anti-laminin (LSL), anti-podoplanin/gp38 (HG-19), FITC-peanut agglutinin (PNA; Sigma-Aldrich), anti-FcγRII/III (2.4G2), anti-CD44 (KM201), anti-gp38 (8.1.1; Ref. 27), anti-FDC-M2 (209; Ref. 28), and biotin-anti-BP-3 Ab (29) (hybridoma supernatants or purified Abs); as secondary reagents, PE-anti-rat IgG, allophycocyanin-anti-rat IgG, biotin-anti-rat IgG, FITC-anti-hamster IgG (Caltag Laboratories), FITC-anti-rabbit IgG, Cy5-anti-rabbit IgG (The Jackson Laboratory), Alexa Fluor 488-anti-rabbit IgG, Alexa Fluor 488-anti-goat IgG, PE-streptavidin, and allophycocyanin-streptavidin (Molecular Probes). Abs against integrin α_L (KBA2) and α_4 (PS/2) were purified from hybridoma supernatants.

Immunohistochemistry

Tissues isolated from animals were embedded in OTC compound (Sakura Finetechnical) and then frozen in liquid nitrogen. Frozen sections (10-μm thick) were fixed with cold acetone. BLS12 cells plated on chamber slides (Nalgen Nunc International) with or without coculturing or factor treatment were fixed with 3% paraformaldehyde-PBS and then permeabilized with 0.2% Triton X-100. After blocking with 1% BSA/0.05% Tween 20-PBS, sections or cells were stained with Abs. Nuclear DNA was stained with 4,6′-diamidino-2-phenylindole (DAPI; Sigma-Aldrich). Sections or cells were examined using a confocal laser scanning microscope (TSC-SP2; Leica). Digital images obtained were prepared using Adobe Photoshop software (Adobe Systems).

Flow cytometry

BLS12 cells were harvested from culture dishes using 0.02% EDTA-PBS. After blocking with PBS containing 1% BSA, the cells were stained with Abs by direct or indirect methods, counted using a FACSCalibur flow cytometer (BD Biosciences), and analyzed using CellQuest software (BD Biosciences).

ELISA

Confluent BLS12 cells in 24-well culture plates were stimulated with mouse TNF-α (10 ng/ml; PeproTech), human TNF-β (LTα3, 10 ng/ml; PeproTech), and/or polyclonal goat anti-mouse LTβR Ab (0.5 μg/ml; R&D Systems). Production of CXCL13 and CCL19 in culture supernatants was detected by sandwich ELISA using DuoSet (R&D Systems) according to the manufacturer's recommendations.

RT-PCR analysis

RT-PCR analysis was performed as described previously (30). Specific primer pairs used in this study were as follows: GAPDH, 5′-CCATCACCATCTTCCAGGAG-3′ and 5′-CCTGCTTCACCACCTTCTTG-3′; CXCL13, 5′-TTGAACTCCACCTCCAGGCA-3′ and 5′-CTTCAGGCAGCTCTTCTCTT-3′; CCL5, 5′-TCTGAGACAGCACATGCATC-3′ and 5′-CCTAGCTCATCTCCAAATAG-3′; CCL19, 5′-GCACACAGTCTCTCAGGCTC-3′ and 5′-CTCTCTTCTGGTCCTTGGTT-3′; CCL21, 5′-AGCTATGTGCAAACCCTGAG-3′ and 5′-TCATAGGTGCAAGGACAAGG-3′; CXCL12, 5′-AAACCAGTCAGCCTGAGCTAC-3′ and 5′-TTACTTGTTTAAAGCTTTCTC-3′; IL-7, 5′-TCCTCCACTGATCCTTGTTC-3′ and 5′-TTGTGTGCCTTGTGATACTG-3′; and BAFF, 5′-TCGTGGAATGGATGAGTCTG-3′ and 5′-TCTGTTTCCTCTGGTCCCTG-3′.

Lymphocyte adhesion to BLS12

The in vitro adhesion assay was performed as described previously, with slight modifications (31). BLS12 cells were plated on fibronectin-coated (20 μg/ml) 96-well plates and cultured for 2–3 days to form monolayers. Twenty-four hours before the assay, the confluent BLS12 monolayer was stimulated with agonistic anti-LTβR Ab (0.5 μg/ml). Primary lymphocytes were labeled with 1 μg/ml 2′,7′-bis-(2-carboxyethyl)-5-(and-6)-carboxyfluorescein (Molecular Probes) at 37°C for 20 min. Labeled lymphocytes were applied to the BLS12 monolayer at 5×10^5 cells/well and incubated at 37°C for 30 min with or without 20 μg/ml blocking Abs. Alternatively, lymphocytes were pretreated with 0.2 μg/ml pertussis toxin (PTx) or B oligomer (Calbiochem) at 37°C for 2 h. Nonadherent cells were removed by five consecutive washes. Input and bound cells were measured using a fluorescence multiwell plate reader (Cytofluor4000; Applied Biosystems).

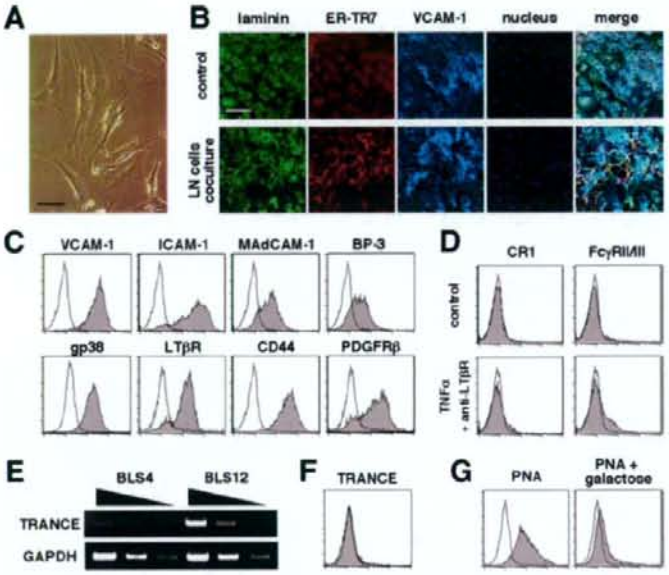

FIGURE 1. Basic characterization of adult LN stromal cell line BLS12. *A*, BLS12 cells show fibroblastic morphology. A phase-contrast view of growing cells on plastic dishes is shown. Bar, 50 μm. *B*, BLS12 produces reticular matrix via contact with lymphocytes. BLS12 monolayers on chamber slides were cocultured with LN cells for 6 days. After fixation and permeabilization, cells were stained with Abs against laminin, ER-TR7, and VCAM-1, counterstained with DAPI, and examined by confocal microscopy. Bar, 100 μm. *C*, Cell surface markers expressed on BLS12 cells. EDTA-harvested BLS12 cells were stained for the indicated surface markers and analyzed by flow cytometry. Histograms show overlays of stained (filled histograms) and control (open histograms). *D*, No significant expression of CR1 or FcγRII/III is induced in BLS12 by dual signaling through TNFR and LTβR. Cells were stimulated with or without TNF-α (10 ng/ml) and agonistic anti-LTβR Ab (0.5 μg/ml) for 2 days. Harvested cells were stained for CR1 and FcγRII/III and analyzed by flow cytometry. *E* and *F*, BLS12 constitutively expresses TRANCE mRNA, but TRANCE protein is undetectable at the cell surface. The transcript for TRANCE was detected by RT-PCR (*E*). The amounts of PCR products amplified from 5-fold serial dilutions of BLS12 cDNAs were standardized relative to GAPDH. Another reticular cell line, BLS4, was used as a control and showed little expression of TRANCE mRNA. Cell surface TRANCE protein was analyzed by flow cytometry (*F*). *G*, BLS12 displays carbohydrates recognized by PNA. Cells were stained with FITC-PNA in the presence or absence of 0.2 M galactose and analyzed by flow cytometry. Addition of galactose markedly diminishes the PNA binding to BLS12 cells, indicating that most of the binding is mediated by the lectin activity of PNA.

B cell migration on BLS12 monolayer

BLS12 cells were seeded on fibronectin-coated (20 μg/ml) ΔT dish (Bioptechs) and cultured for at least 5 days to construct a monolayer. The confluent BLS12 monolayer was stimulated with agonistic anti-LTβR Ab (0.5 μg/ml) for 24 h. Primary B cells (5×10^5) were loaded onto activated BLS12 monolayers in RPMI 1640 medium supplemented with 8% FCS and 10 mM HEPES. After 3 h of incubation, phase-contrast images were obtained every 30 s for 30 min at 37°C on a LSM510 confocal laser microscope (Zeiss) equipped with a heating stage system for ΔT dishes (Bioptechs). Blocking Abs (final concentration, 20 μg/ml) were added 30–60 min before commencement of image capture. Alternatively, lymphocytes were pretreated with 0.2 μg/ml PTx or B oligomer (Calbiochem) at 37°C for 2 h. Image data were analyzed using Image-Pro Plus software (Media Cybernetics). In each field, 40–50 randomly selected cells were manually tracked to measure mean velocity and displacement from starting point.

Fc chimeric proteins

LTβR-Fc and Il-6 TCRVα-Fc chimeric proteins were produced as described previously (26, 30). Specifically, X63.653 myeloma cells were stably transfected with each vector construct, and chimeric proteins were purified from culture supernatants or ascites fluid using a protein G- Sepharose column (Amersham Biosciences). Mice were i.v. injected weekly with 100–200 μg of chimeric proteins and were sacrificed 2–4 wk later to obtain SLOs.

Results

Stromal cell line BLS12 is reticular fibroblast with the ability to produce CXCL13 upon LTβR-NIK signaling

We previously established a series of stromal cell lines from adult mice LNs (4). One of these, BLS12, showed typical fibroblastic morphology (Fig. 1*A*). When cocultured with lymphocytes, BLS12 showed the ability to produce ECM meshwork that contains laminin, fibronectin, and ER-TR7-Ag (Fig. 1*B* and data not shown), indicating that this cell line preserves FRC features. It is worth noting that BLS12 constitutively expressed MAdCAM-1 and BP-3 (CD157), in addition to FRC markers such as VCAM-1, ICAM-1, and gp38 (podoplanin) on the surface (Fig. 1*C*). BLS12 also expressed LTβR, CD44, and a mesenchymal marker, PDGFRβ (Fig. 1*C*). In contrast, FDC markers CR1 (CD35) and FcγRII/III (CD16/32) were undetectable, and were virtually uninducible even when the cells were simultaneously stimulated with TNF-α and agonistic anti-LTβR Ab (Fig. 1*D*) or cocultured with lymphocytes (data not shown). Although surface expression of TRANCE protein was undetectable in BLS12, the mRNA was readily detected, in contrast to another FRC line, BLS4, in which TRANCE mRNA was almost undetectable (Fig. 1, *E* and *F*). In addition, BLS12 cells displayed cell surface carbohydrates recognized by PNA (Fig. 1*G*).

Of prime importance, BLS12 cells exhibited the ability to express CXCL13 upon LTβR ligation and a substantial amount of CXCL13 protein was detected in the culture supernatant (Fig. 2, *A* and *B*). Although TNFR ligands, TNF-α or LTα3, did not induce CXCL13 on their own, both of these cytokines markedly augmented the LTβR-induced CXCL13 expression. The stable overexpression of NIK in BLS12 cells resulted in spontaneous CXCL13 production (Fig. 2, *C* and *D*), suggesting that excessive NIK is sufficient for inducing CXCL13 in this cell context. We

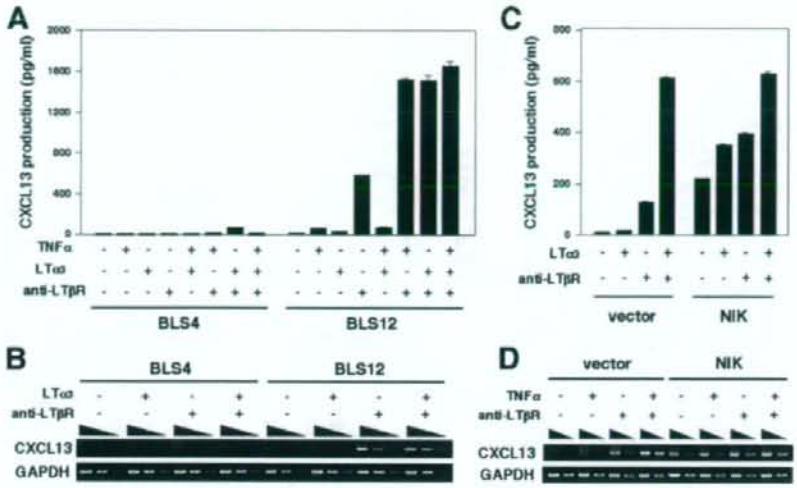

FIGURE 2. BLS12 produces CXCL13 upon LTβR-NIK signaling. *A* and *B*, BLS12 but not BLS4 produces CXCL13 in response to LTβR ligation. BLS cells were stimulated with TNF-α, LTα3, anti-LTβR Ab, or combinations of these stimulants for 5 days. CXCL13 protein in the supernatant was measured by ELISA (*A*). The results are shown as means ± SD. Note that TNF-α and LTα3 used in our experiments exert almost equivalent enhancing effects on LTβR-mediated CXCL13 production. The transcript for CXCL13 was detected by semiquantitative RT-PCR analysis 2 days after the stimulation (*B*). *C* and *D*, Overexpression of NIK induces spontaneous CXCL13 production in BLS12. BLS12 stably transfected with control (vector) or NIK was stimulated with LTα3 (or TNF-α), anti-LTβR Ab, or combinations thereof for 2 days. CXCL13 expression was analyzed by ELISA (*C*) and RT-PCR (*D*).

also detected CCL19 mRNA only when BLS12 cells were simultaneously stimulated with LTα3 (or TNF-α) and agonistic anti-LTβR Ab (Fig. 3); however, the secreted protein level was nearly undetectable (data not shown). In contrast, no CCL21 expression could be detected irrespective of the presence or absence of any stimuli tested (data not shown). BLS12 cells also expressed factors required for lymphoid homeostasis, such as IL-7, BAFF, and CXCL12 (Fig. 3).

BLS12 supports the motility of primary B cells

To investigate the interaction between lymphocytes and BLS12, we first examined the adhesion of B cells to BLS12 cells. Approximately 20% of freshly isolated B cells adhered to an unstimulated BLS12 monolayer after several hours of incubation; this adhesion was much more effective than to BLS4 monolayer, which bind only below 5% of primary B cells (Fig. 4*A*). Prestimulation of BLS12 cells with agonistic anti-LTβR Ab slightly augmented the adhesion. The adhesion of B cells to BLS12 cells was markedly inhibited by anti-α_4 integrin Ab and weakly inhibited by anti-α_L integrin Ab (Fig. 4*B*). The mixture of the two Abs blocked almost all of the adhesion. The pretreatment of B cells with PTx also dramatically inhibited the adhesion, while B oligomer, the noncatalytic subunit of PTx, showed virtually no effect (Fig. 4*C*). Taken together, these data indicate that Gαi-dependent signaling and integrins mediate B cell adhesion to BLS12 in this experimental setting.

We next addressed whether primary B cells are motile on the surface of BLS12. For this purpose, B cells were loaded onto a monolayer of LTβR-stimulated BLS12 and incubated for several hours in a heating chamber system. Under such conditions, time-lapse image analysis revealed that the B cells actively migrated on BLS12, showing significant displacement from the starting point with an average velocity of 5–6 μm/min (Fig. 4, *D–F*, and video 1[4]). Addition of Abs against integrins (Fig. 4, *D–F*, and videos 2 and 3) or pretreatment of B cells with PTx (Fig. 4, *G–I*, and videos 4 and 5) significantly reduced both velocity and displacement, suggesting that the motility of B cells on BLS12 is partially mediated by Gαi-dependent signaling and integrins, while residual motile activity is driven by unknown cues. Taken together, the data demonstrate that BLS12 has the unique property of supporting the motility of B cells.

Marginal reticular cell (MRC) layer is a unique stromal network in adult LNs

From the aforementioned results, we noticed that BLS12 cells share some characteristics with FDCs, e.g., the expression of MAdCAM-1 and BP-3, LTβR-dependent CXCL13 production, and the capacity to support B cell behavior. However, these cells express neither CR1 nor FcγRII/III, both of which are crucial and functional markers of FDCs (32). In addition, FDCs are generally weak producers of reticular fibers (3). These facts prevent us from considering BLS12 to be a FDC line.

To obtain a clue about the origin of BLS12, we examined in detail the stromal structure of the LNs. As has been well established, the FDC network was clearly observed at the center of the follicles, which

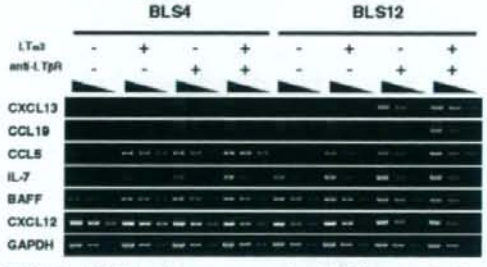

FIGURE 3. BLS12 cells express some lymphoid homeostatic factors. BLS4 and BLS12 cells were stimulated with LTα3, anti-LTβR Ab, or combinations thereof for 2 days. Transcripts for the indicated factors were detected by RT-PCR. The amounts of PCR products amplified from 5-fold serial dilutions of cDNAs were standardized relative to GAPDH.

[4] The online version of this article contains supplemental material.

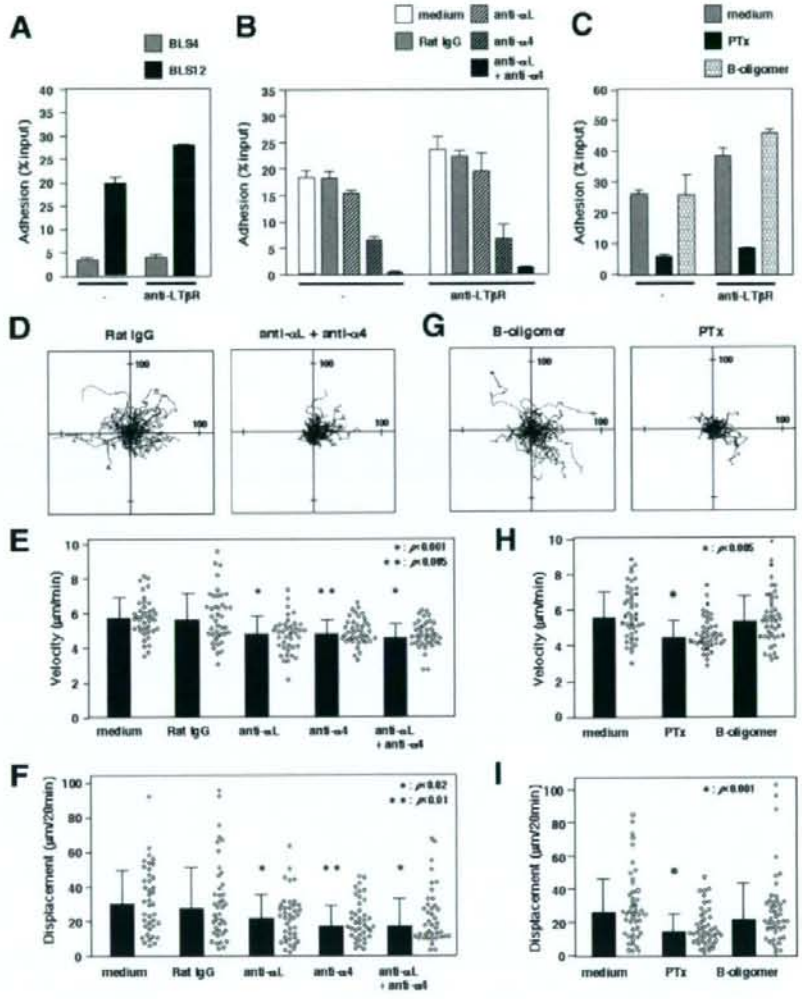

FIGURE 4. BLS12 supports the migration of primary B cells. *A*, Primary B cells adhere to BLS12. Adhesion of fluorescence-labeled B cells to BLS12 or BLS4 monolayer after 3 h of incubation was measured. Results are shown as means ± SD. *B*, The adhesion of B cells to BLS12 is integrin dependent. B cell adhesion to BLS12 in the presence or absence of Abs (20 μg/ml) was measured. *C*, Gαi-dependent adhesion of B cells to BLS12. B cells were pretreated with PTx or B oligomer and adhesion to BLS12 was measured. *D–F*, BLS12 supports the motility of B cells, which is partially inhibited by Abs against integrins. *D*, Trajectory of B cells with control IgG (*left*) or anti-integrin Abs (*right*). Each line represents a single cell's track over a 20-min time span recorded. Units are in micrometers. *E* and *F*, Anti-integrin Abs partially inhibit the motility of B cells. Each dot represents the average velocity (*E*) and displacement (*F*) of single cells. Columns represent medians ± SD of the population and asterisks indicate significantly different from control rat IgG. *G–I*, Pretreatment of B cells with PTx but not B oligomer partially inhibits the motility on BLS12. *G*, Trajectory of B cells pretreated with B oligomer (*left*) or PTx (*right*). Asterisks indicate significant differences from control.

highly expressed CR1, MAdCAM-1, BP-3, and CXCL13, as well as VCAM-1, ICAM-1, and gp38 (Fig. 5*A*). The nuclear accumulation of RelB in this region was also evident (Fig. 5*Ad*). All of the markers overlapped well in the follicular center. During the course of careful examinations, we found that there was a notable stromal cell layer at the outer margin of the cortex, i.e., the lining of the subcapsular sinus (SCS). This cell layer was brightly positive for MAdCAM-1, CXCL13, BP-3, VCAM-1, ICAM-1, and gp38, but not present in paracortical and medullary sinuses (Fig. 5*A*, red arrows). At most, a faint expression of CR1 was detected in this region. Stromal cells in this restricted area strongly expressed TRANCE, in contrast with the FDC network, which was barely stained for TRANCE (Fig. 5*Af*). Higher magnification views revealed that the layer is composed of a kind of reticular cell network (Figs. 5*B*), which extends several 10s of micrometers from the abluminal side of the SCS immediately underneath the layer of LYVE-1$^+$ lymphatic endothelial cells and the basement membrane-like ECM "floor," indicated by laminin and ER-TR7 (Fig. 5*C*). CXCL13 was detected in a filamentous pattern concurrent with the network (Fig. 5*Ba*). Nuclear RelB accumulation and PNA binding were also evident in this stromal layer (Fig. 5*Ad* and data not shown). Taking these observations together, we concluded that this specialized type of reticular cells represents a distinct population from stromal cells in the other regions, including FDCs and T zone FRCs, and hence designated these cells the MRCs (Fig. 5*D*).

MRC layer is a stromal structure common to different types of SLOs

It is well known that MAdCAM-1$^+$ FRCs, termed the marginal sinus-lining cells, encircle the inner lymphoid sheath of the splenic white pulp (Fig. 6*A*). This stromal layer expressed almost the same marker set with MRC in LNs, including CXCL13, TRANCE, BP-3, gp38, RelB, PNA-binding carbohydrates, laminin, and ER-TR7 (Fig. 6*A* and data not shown), suggesting that reticular cells aligned in this region are equivalent to LN MRCs. The layer was more obvious in the outer margin of the follicles (Fig. 6*A*, arrows) than in the interfollicular channel region (Fig. 6*A*, asterisks). MRC-like stromal networks were also observed in mucosal SLOs such as PPs, NALTs, ILFs (Fig. 6, *B–D*), and cecal lymph patches (data not shown). In all cases, MRC-like cells constituted reticular

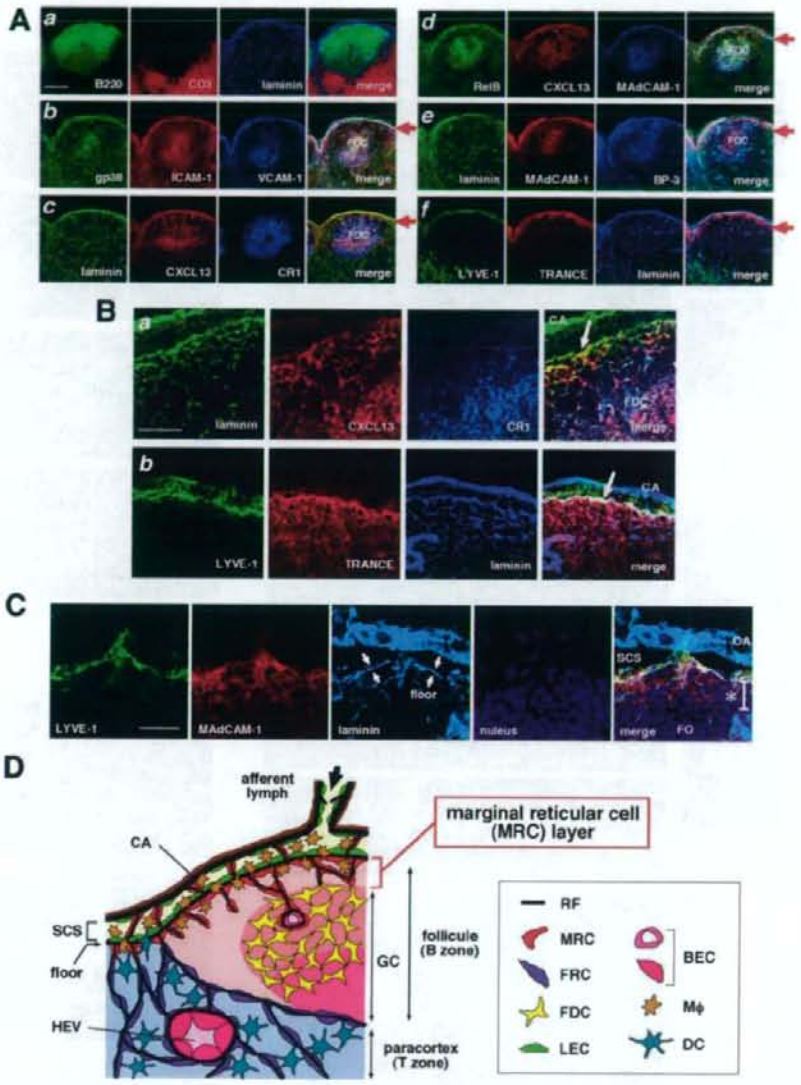

FIGURE 5. A unique reticular stromal layer in the outer margin of adult LN. *A*, Stromal markers are highly expressed in the subcapsular region of LNs. Sections of LNs were stained for various markers and examined by confocal microscopy. Outer cortical regions of the LNs are shown. Red arrows indicate SCS lining. Note that the network of FDCs is present in the center of follicles with high expression of all markers other than TRANCE. Bar, 200 μm. *B* and *C*, Specialized stromal cells constitute the reticular network underneath SCS (arrows in *B* and an asterisk in *C*). Higher magnification views of the subcapsular regions of LNs are shown. Arrows in *C* indicate basement membrane-like floor in the SCS lining. Bars, 50 μm in *B* and 20 μm in *C*. *D*, Schematic representation of MRC layer and the cortical stromal structure of the LNs. Various stromal cells of mesenchymal, endothelial, and myeroid origins, as well as matrix components are included, while lymphocytes are omitted for simplification. The MRC layer is located at the cortical side of the SCS lining, underneath the single layer of lymphatic endothelial cells that covers the luminal surface of the SCS. BEC, Blood endothelial cell; CA, capsule; FO, follicle; GC, germinal center; HEV, high endothelial venule; LEC, lymphatic endothelial cell; Mϕ, macrophage; RF, reticular fiber.

layers restricted to the subepithelial dome region immediately beneath the follicle-associated epithelium (FAE; Fig. 6*E*). In contrast, a MRC-like population was not found in ectopic lymphoid tissues in the stomach induced in mouse models for gastric autoimmunity (30, 33) (data not shown). These data indicate that the MRC layer is a common stromal structure in SLOs.

LTo cells in the marginal area of LN anlagen expand to form the MRC layer during postnatal development

Given that MRCs and LTo stromal cells share many markers, we speculated that there is some relationship between the two mesenchymal lineages. To address this issue, we examined the transitional process of stromal architecture from anlagen to postnatally developing SLOs. A structural examination of fetal LN anlagen has already been reported (34) and the authors showed that ICAM-1^{high}VCAM-^{high} MAdCAM-1^{high} (IVM^{high}) LTo cells expressing chemokines and TRANCE are concentrated in the outer region of the anlagen surrounded by LYVE-1$^+$ lymphatic vasculature, while IVM^{low} cells are localized in deeper regions. We confirmed similar histology of LNs on the day of birth, at which time the LNs still retain the characteristics of anlagen, as few lymphocytes have yet migrated (Fig. 7*A*). CD4$^+$CD3$^-$ LTi cells accumulated in the outer region of anlagen adjacent to presumptive SCS, where stromal cells highly expressing VCAM-1 and ICAM-1 formed a dense layer (Fig. 7*A*, *a* and *b*). In addition to blood vessels, these LTo also expressed MAdCAM-1 (Fig. 7*Ac*). Although TRANCE staining illuminated the whole anlage, a group of stromal cells with higher TRANCE expression clearly delineated the boundary of the lymphatic sinus (Fig. 7*Ad*). A faint signal for CXCL13 was detected in the same cells (Fig. 7*Ac*). Overall, the LN anlagen seem to be segregated into roughly outer and inner parts during ontogeny, and the stromal cells in the former exhibit a phenotype typical of LTo.

At day 6, the size of LNs markedly increased as the influx of lymphocytes and their compartmentalization in the cortical area

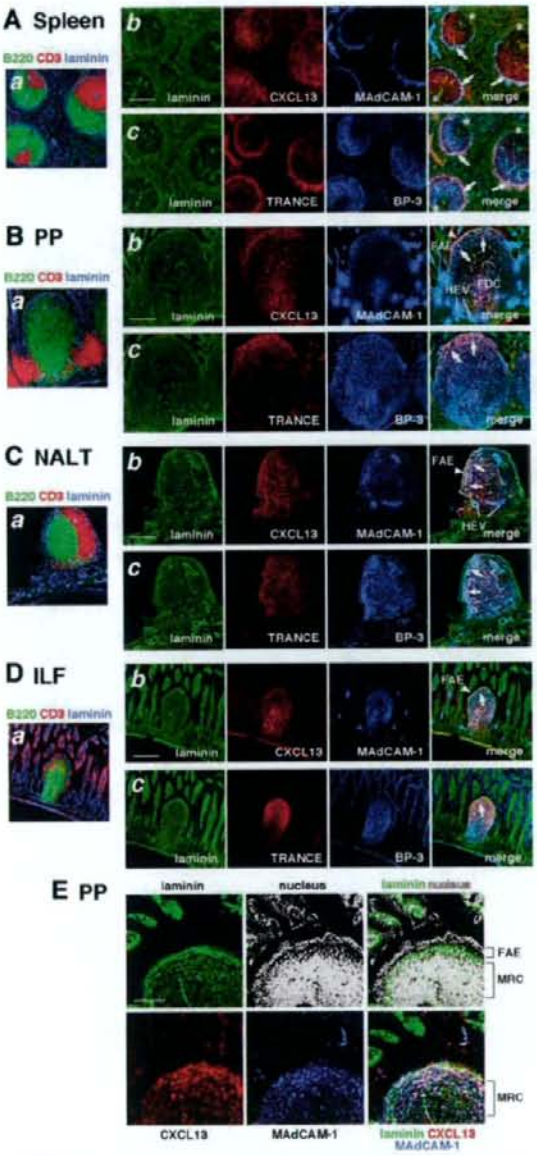

FIGURE 6. MRC layers are present in particular regions of various SLOs. *A*, Reticular stromal cells in the marginal sinus lining of splenic white pulp show characteristics of MRCs. Serial sections of spleen were stained for various markers and examined by confocal microscopy. A composite image of a section stained for laminin, CD3, and B220 shows tissue architecture and lymphocyte localization (*a*). Well-known MAdCAM-1$^+$ marginal sinus-lining cells highly express the set of MRC markers (arrows). The MRC-like layer is obscure in the interfollicular channel region (asterisks). *B–D*, Reticular stromal cells in the subepithelial dome of PP (*B*), NALT (*C*), and ILF (*D*) show characteristics of MRCs (arrows). Arrowheads indicate FAE. Luminal surface of the epithelia is often nonspecifically stained by anti-CXCL13 Ab. Higher expression of MAdCAM-1 is observed in FDCs and high epithelial venules. Bars, 200 μm. *E*, Higher magnification view of the subepithelial dome region in the PP. Section was stained with Abs against laminin, CXCL13, and MAdCAM-1 and counterstained with DAPI for the visualization of the nucleus. MRC network is localized immediately underneath the FAE layer (laminin$^-$ CXCL13$^-$MAdCAM-1$^-$). Bar, 100 μm.

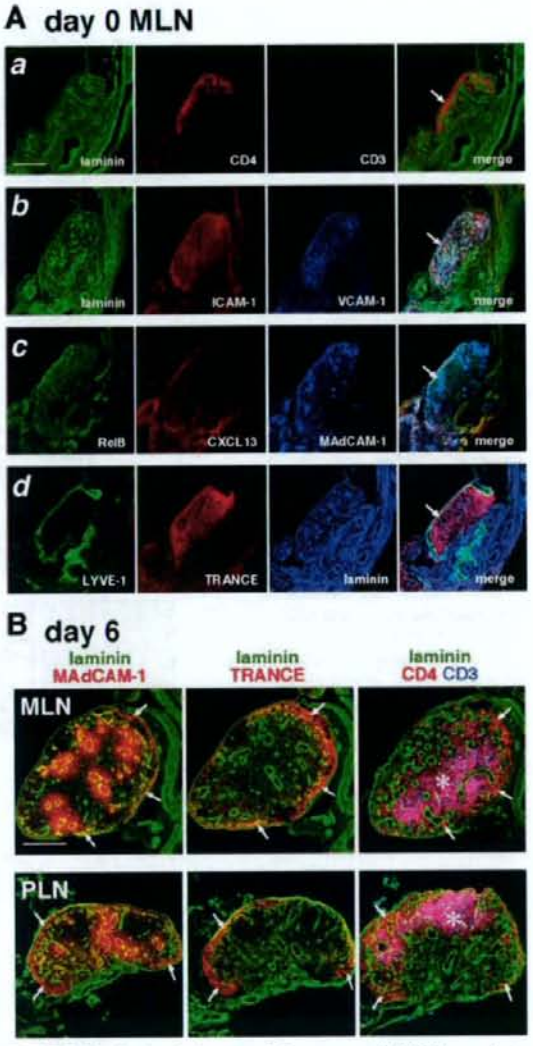

FIGURE 7. Continuity between LTo stroma and MRC layer during postnatal development of LNs. *A*, Stromal architecture of day 0 mesenteric LNs (MLN). Serial sections of mesentery, including mesenteric LNs from day 0 mouse, were stained for the indicated markers. CD4$^+$CD3$^-$ LTi cells (*a*) are accumulated in the marginal region of the anlagen, where LTo stromal cells with higher expression of ICAM-1, VCAM-1 (*b*), MAdCAM-1 (*c*), and TRANCE (*d*) are condensed underneath presumptive SCS (arrows). Bar, 200 μm. *B*, Expansion of the MRC layer in postnatally growing LNs. Composite images of day 6 mesenteric LNs and peripheral LNs (PLN) are shown. Presumptive MRC layers highly expressing MAdCAM-1 and TRANCE are observed at the outermost regions (arrows in *left* and *middle panels*). In the *right panels*, CD4$^+$CD3$^+$ mature T cells accumulate in the inner cortex (asterisks), while CD4$^+$CD3$^-$ cells are still present in the outer cortex (arrows). Note that MAdCAM-1 is still expressed by blood vessels even in peripheral LNs at this time. Bar, 200 μm.

began (Fig. 7*B*). The expression of MAdCAM-1 and TRANCE was markedly reduced in the developing paracortex and medulla, while the outermost part still retained high expression of the two molecules in conjunction with the colonization of CD4$^+$CD3$^-$ cells. These observations are consistent with the idea that, with the

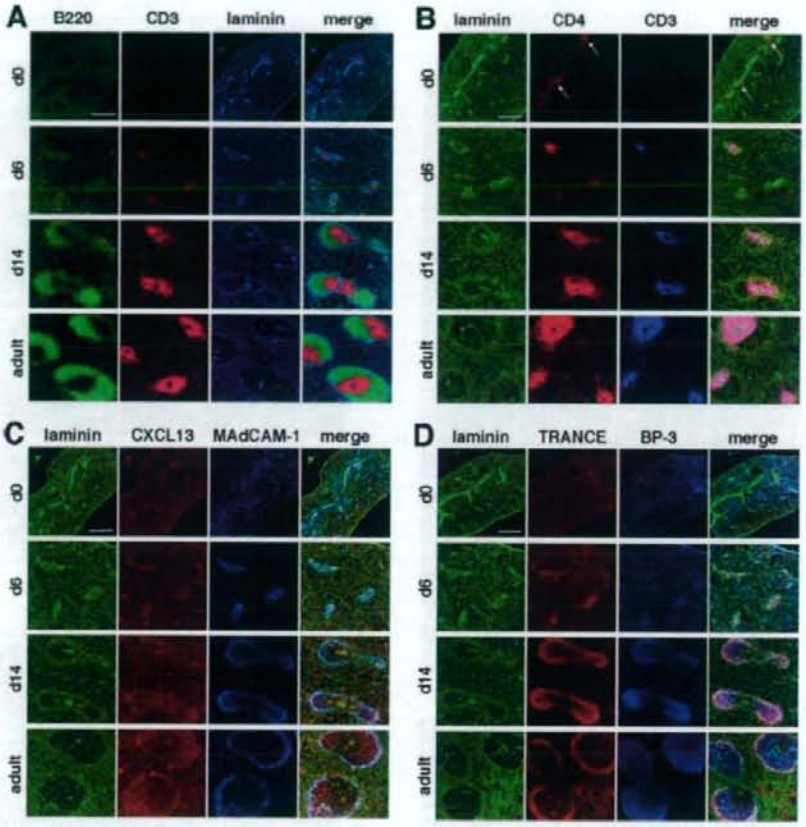

FIGURE 8. Development of the white pulp in spleen. Spleen sections from days 0, 6, and 14 and adult mice were stained for the indicated markers and examined by confocal microscopy. MRC layer/marginal sinus-lining structure expands and becomes prominent as lymphocytes are accumulated. In day 0 spleen, $CD4^+CD3^-$ LTi-like cells are concentrated at presumptive white pulp surrounding large blood vessels (arrows in *B*). Bars, 200 μm.

expansion of the organ, LTo stromal cells subsequently form a thin MRC layer in the tissue periphery.

An analogous process occurred in the area surrounding the central artery in the developing spleen, in which a stromal layer similar to LTo/MRCs expanded outward as lymphocytes accumulated in presumptive white pulp; eventually, this layer constituted the lining of the marginal sinus (Fig. 8). Interestingly, MAdCAM-1^+ mesenchymal cells showed relatively diffuse distribution in the day 0 spleen, but thereafter became concentrated around the artery at day 6 and then expanded to form the MRC layer. Accordingly, there is a dynamic redistribution of MRC lineage in the developing spleen.

Maintenance of MRC property requires LTβR signaling

To address the role of LTβR signaling in the maintenance of the MRC layer in mature SLOs, LTβR-Fc chimeric protein was injected into adult mice, and SLOs were examined after 2–4 wk of weekly administration of the chimeric proteins. No discernable alterations in the architecture of SLOs were observed in control experiments in which mice were injected with II-6 TCRVα-Fc chimeric protein (30) or PBS compared with untreated animals (Fig. 9 and data not shown). Consistent with previous reports, the structure of splenic white pulp (in particular, follicular assembly) was disorganized as a result of LTβR-Fc treatment (35, 36) (Fig. 9*A*). FDC networks also disappeared (data not shown). LTβR-Fc treatment abolished MAdCAM-1 expression and the typical boundary structure of the marginal sinus, which also caused the complete disappearance of the MRC layer highlighted by CXCL13, TRANCE, and BP-3 staining. Similar views were obtained in the spleen in *aly/aly* mice, which bear a point mutation in NIK (37) (Fig. 9*A*), and the observations are in good accordance with a previous report showing the absence of sinus-lining FRCs and MAdCAM-1 expression in the *aly/aly* spleen (38). These data indicate that the maintenance of the MRC layer in the spleen strongly depends on LTβR-NIK signaling.

Although LTβR-Fc treatment dramatically diminished the expression of CXCL13 and MAdCAM-1 in the MRC layer of the LNs, TRANCE expression was comparable to or slightly reduced compared with that in control LNs; furthermore, we found no remarkable alteration in the structure of the SCS (Fig. 9*B*). As FDC networks indicated by CR1 and FDC-M2, which are highly depending on LTβR signaling, disappeared (data not shown), circulating LTβR-Fc protein was suggested to reach a high enough level to block the pathway. This suggests that TRANCE expression in MRCs is independent of LTβR-signaling or another TRANCE-expressing cell types still exist in the case of LNs, although some MRC properties still depend on this pathway. It is also clear that the LTβR dependence in MRC layers differs among SLOs.

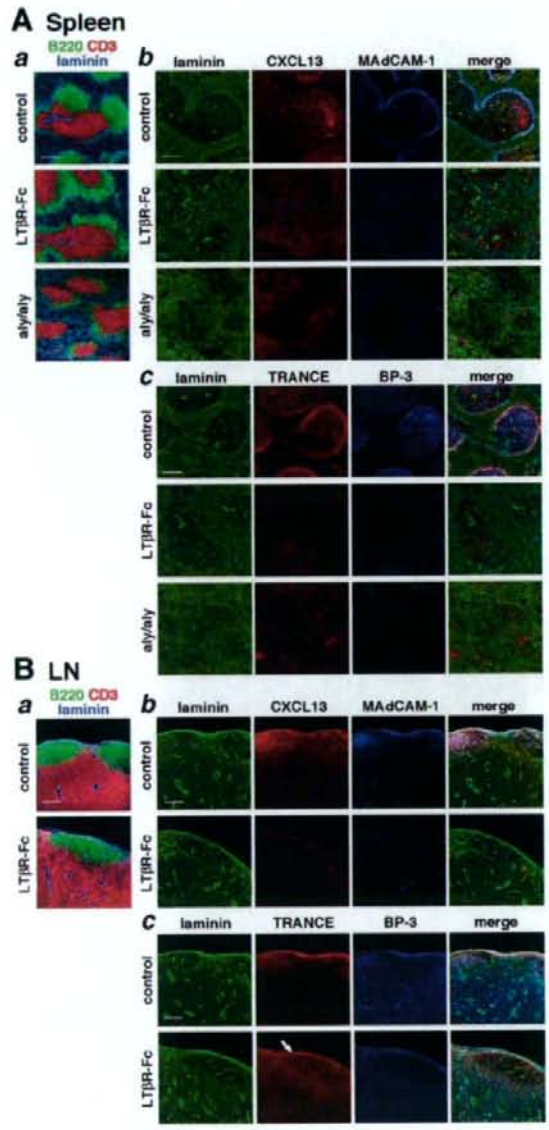

FIGURE 9. LTβR signaling is involved in the maintenance of MRC features. *A*, Inhibition of LTβR signaling or the absence of NIK activity abolishes MRC layer/marginal sinus-lining structure in the splenic white pulp. Spleens from control (Vα-Fc)-treated mice, LTβR-Fc-treated mice, or *aly/aly* mice were examined for the indicated markers. Representative images for the localization of T and B cells (*a*) and stromal structures (*b* and *c*) in each experiment are shown. MRC layers are absent in LTβR-Fc-treated or *aly/aly* mice spleen. Follicular structures are severely disorganized as well (*a*). *B*, Inhibition of LTβR signaling abolishes some markers but has little influence on TRANCE expression in LN MRCs. LN sections from control (Vα-Fc)- or LTβR-Fc-treated mice were examined for the indicated markers. Substantial expression of TRANCE is still retained in the MRC layer of LTβR-Fc-treated mice (arrow). Bars, 200 μm.

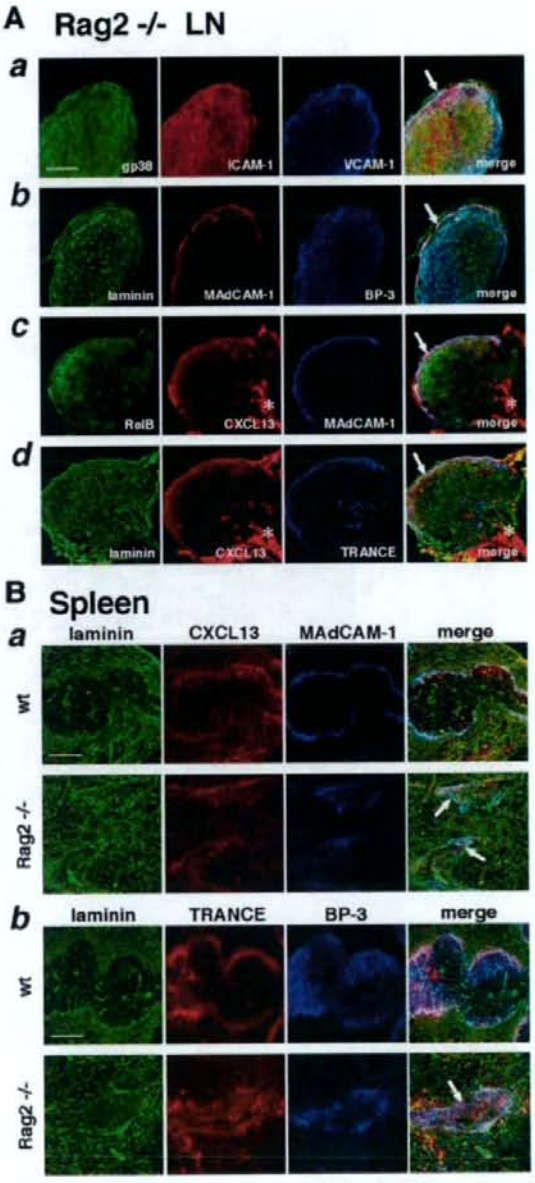

FIGURE 10. MRC layer is present in Rag2$^{-/-}$ mice SLOs. *A*, Stromal cells expressing MRC markers can be observed at the SCS lining in the rudimental LNs of Rag2$^{-/-}$ mice (arrows). Peripheral LNs from Rag2$^{-/-}$ mice were examined for the indicated markers. Adipose tissues attached to the LNs are nonspecifically stained by anti-CXCL13 Ab (asterisks). *B*, Stromal sacks that express MRC markers are observed at the rudimentary white pulp surrounding the central splenic artery in Rag2$^{-/-}$ mice (arrows). Spleens from wild-type (wt) and Rag2$^{-/-}$ mice were examined for the indicated markers. Bars, 200 μm.

Lymphocytes are dispensable for the formation of MRC layer

To address whether lymphocytes are required for the MRCs in adult SLOs, we next examined Rag2$^{-/-}$ mice. Rag2$^{-/-}$ mice have rudimentary LNs due to the lack of lymphocytes; nonetheless, we could clearly observe the MRC layer in the subcapsular region of each LN, in which weak but significant expression of CXCL13 was present (Fig. 10*A*). Thus, at least two compartments, i.e., the MRC layer and inner stroma, are unambiguously formed even in

the LNs from lymphocyte-deficient animals. Likewise, we observed reduced but significant expression of MRC markers at the sheath-like stromal structure surrounding the artery in the $Rag2^{-/-}$ mice spleen (Fig. 10*B*). These findings indicate that lymphocytes are not essential for the differentiation and maintenance of MRCs.

Discussion

In this study, the characterization of the lymphoid stromal cell line BLS12 prompted us to notice a unique lymphoid stromal population, MRC. MRC could be classified into a novel category of mesenchymal lineage common to adult SLOs, defined as the population of specialized reticular fibroblasts localized at a particular area of the tissues. These cells exhibit high expression of VCAM-1, ICAM-1, MAdCAM-1, CXCL13, TRANCE, BP-3, and gp38, as well as various reticular matrix components. Although FDCs show a similar marker set, they exhibit high expression of CR1 but low or no TRANCE, whereas MRCs express TRANCE but little or no CR1. Furthermore, FDCs do not generally produce typical reticular structure such as the one that surrounds the ECM fiber to form the conduit. Since the phenotypical characteristic of BLS12 shows good agreement with the criteria for MRC, we consider this cell line to be of MRC origin. However, there are some discrepancies between the nature of BLS12 and MRCs. For instance, BLS12 cells in culture constitutively display VCAM-1, ICAM-1, and MAdCAM-1, whereas in vivo the expression of these molecules is regulated by LTβR signaling. In addition, TRANCE protein is undetectable in BLS12, although TRANCE mRNA is readily detected. Immortalization and expansion in vitro presumably caused these alterations in BLS12.

Now that MRCs have been added to the list of stromal cells, every SLO turns out to be composed of at least three different types of mesenchymal stromal cells, i.e., FRCs in T zone, FDCs, and MRCs. Among these, the former two, FRCs expressing CCL19/CCL21 in the T zone and FDCs expressing CXCL13 in the follicular center, have been established as major anatomical backbones for the T and B compartments, respectively (7). It was recently demonstrated that these stromal networks support lymphocyte movement, acting as guidance footholds (39). Although the medulla of LNs and the marginal zone of the spleen are supported by types of FRC subsets distinct from those in the T zone (3, 14), these populations are not to be included in the common elements because they reside in varying anatomical compartments depending on SLO type. T zone FRCs and follicular FDCs are closely associated with the corresponding lymphocyte subsets. In addition, both of these types of stromal cells are induced in chronic inflammatory diseases, even in ectopic lymphoid tissues (30, 33, 40, 41). Therefore, we would suggest that the existence of mature lymphocytes induces the differentiation and maintenance of these stromal cells. In accordance with this, no obvious subcompartments supported by these stromal lineages are observed in $Rag2^{-/-}$ mice SLOs, whereas adoptive transfer of lymphocytes restores them (Ref. 1 and our unpublished observation). In contrast, MRCs are probably present in all SLOs, even in $Rag^{-/-}$ mice, but absent in ectopic lymphoid tissues, strongly supporting the notion that MRCs are a developmentally programmed element and tightly fixed to the organ, irrespective of the existence of mature lymphocytes. This notion is consistent with previous observations that organogenesis and even some tissue compartmentalization of SLOs, possibly concomitant with the separation of MRCs from other stromal cells, can occur in SCID mice (42–44).

The fact that MRCs display the set of molecular markers that is also expressed by LTo cells suggests the relevance of them. Indeed, we observed that LTo descendants in the outer margin of the LN anlagen seem to subsequently form the MRC layer. Likewise, periarteriolar LTo-like sheaths in the neonatal spleen gradually expand to form MRC rings, previously known as marginal sinus-lining cells. These observations prompt us to speculate that the organizer-like stromal cells are still present as MRCs in mature SLOs. MRC-like cells are also observed in the apical dome region of mucosal-associated lymphoid organs. These are likely the same cells reported previously as $TRANCE^{+}$ stromal cells in PPs, ILFs, and CPs (45). In general, CPs contain few lymphocytes but are colonized by LTi-like hematopoietic cells and the stromal cells exhibit characteristics similar to LTo/MRC (13, 46). It was recently suggested that ILFs are inducible structures derived from CP in response to the intestinal bacterial flora (13). Therefore, the maturation process of ILFs recapitulates the organogenesis of SLOs in the adult environment.

Based on the findings in this study and slightly modifying the models presented previously (10, 47), we propose following four sequential stages of SLO organogenesis from anatomical and stromal viewpoints (Fig. 11). In the earliest phase (stage I), a developmentally programmed "address code" determines the location of anlagen by attracting LTi cells or converting the adjacent mesenchyme to LTo congregates. Cross-talk between LTi and LTo cells facilitates the maturation of LTo stroma, which further drives a positive feedback loop. As anlagen grow (stage II), the stromal network differentiates into outer (genuine LTo layer?) and inner (presumptive lymphocyte compartment) parts (primary differentiation and compartmentalization of stromal cells). Hashi et al. (43) demonstrated the compartmentalization of the PP anlagen before lymphocyte entry and several other reports also have presented clear pictures showing uneven distributions of LTo and LTi cells within the SLO anlagen (22, 34). After birth (stage III), the influx of lymphocytes begins and the inner part of anlagen is further divided into lymphocyte subcompartments with corresponding adult stromal subsets (secondary differentiation and compartmentalization of stromal cells); meanwhile, the outermost part expands to form the MRC layer. Tissue architecture (stage IV) is maturated in the adult SLO. Continuous LTβR signaling is required for maintenance of the properties of MRCs; however, the dependence on this pathway varies depending on the individual SLO. The administration of LTβR-Fc completely disrupts the marginal sinus structure, with loss of the MRC layer in the splenic white pulp, although this treatment does not lead to the immediate disappearance of the white pulp structure. Likewise, LTβR-Fc partially diminishes markers in LN MRCs, but has little effect on TRANCE expression or overall tissue geometry, suggesting that MRCs are dispensable for the accumulation and compartmentalization of lymphocytes, at least once the construction of SLO architecture has been accomplished.

Although the functional significance of MRCs in adult SLOs remains largely unknown, we consider it important to note that all MRC layers in various SLOs are faced toward the major route of antigenic entry (Fig. 11). DCs capturing Ags in peripheral tissues migrate to the draining LNs via afferent lymph. They first reach the SCS, from which they pass across the MRC layer to enter the paracortex (48). Low-molecular weight soluble Ags can pass the SCS lining, penetrating into the conduit network in the T zone, where they can be picked up by resident DCs (5, 6). Analogously, MRC networks in the subepithelial dome of mucosal SLOs harbor unique DC subsets by which Ags are transported from the FAE to the follicular region (49, 50). In the spleen, blood-borne Ags and immune cells must pass through the marginal stromal layer to enter the inner lymphoid compartment of the white pulp (14). Accordingly, the MRC layer possibly regulates these Ag-transporting pathways. Of note along these lines, follicular B cells in the LN

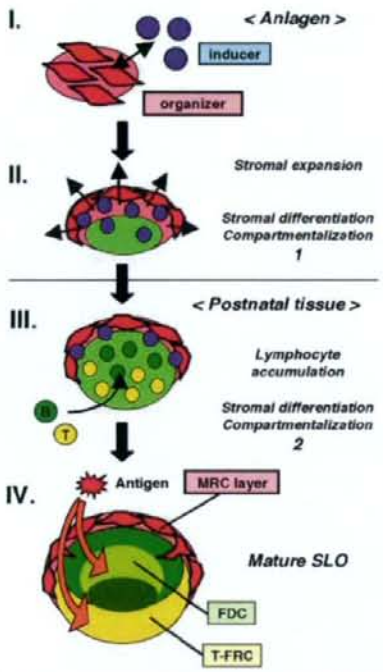

FIGURE 11. A common model for SLO oraganogenesis that progresses through four sequential stages. Stage I: In the earliest step, intimate interaction between organizer mesenchyme and inducer cells forms the SLO anlagen, under the control of an address code specific in embryonic environment. Stage II: As the anlage grows, the stromal compartment is gradually segregated into outer and inner parts, i.e., the presumptive MRC layer and lymphocyte compartments, respectively (primary differentiation and compartmentalization of stromal cells). Stromal cells in the outer part show the organizer phenotype more remarkably. Stage III: After birth, lymphocytes are accumulated in the inner area, in which they are further separated into outer (B cells) and inner (T cells) areas with the differentiation of corresponding stromal lineages (secondary differentiation and compartmentalization of stromal cells); meanwhile, the outermost stromal population proceeds to expand and eventually forms the MRC layer. B cells in the outer cortex are further assembled to form follicles. Stage IV: Mature architecture of adult SLO. In response to antigenic stimuli, a germinal center is occasionally developed in the follicle, with the asymmetry of dark and light zones. Note that common stromal elements in mature SLOs are MRCs, FDCs, and T zone FRCs. Regular tissue architecture is arranged along with a polarity axis directed toward the major route of Ag entry.

directly capture lymph-borne Ags, either in a soluble form penetrated from the SCS or in a particulate form from SCS-resident cells (51–54). As the network of MRCs covers the outer part of the follicle, MRCs are likely to be involved in the Ag transport along this route. It is also likely that the MRC network is the foothold for the migration of B cells in the outer follicle. Intravital two-photon microscopy has shown that B cells in this region are highly motile (52, 53). Lo et al. (55) have demonstrated that lymphocyte entry into the splenic white pulp across the marginal sinus is integrin and $G\alpha i$ dependent. High expression of adhesion molecules in MRCs suggests that their network represents a potential foothold not only for B cells but also for macrophages and DCs. In fact, BLS12 cells display various adhesion molecules and constitutively produce CXCL12; they express CXCL13 in response to LTβR signaling. BLS12 also supports the migration of primary B cells in vitro, which partially depends on $G\alpha i$-mediated signaling and integrins. However, recent studies have shown that integrins are not the major adhesion machinery, at least for the interstitial migration of T cells and DCs within the LN (56, 57). Careful examination of the integrin requirement for the migration of B cells in this area will be required in future studies.

In summary, the MRC layer is a common landmark of mature SLOs; these stromal cells are presumably the adult counterpart of LTo. The organogenesis of SLOs proceeds like a layer-forming reaction. Supposing the LTo/MRC layer as the organizing front of developing SLOs, this is quite reasonable, because the anatomical arrangement of SLOs must necessarily be optimized for capturing and detecting external Ags most efficiently. Since there are multiple mesenchymal lineages, each with distinct functions, tightly integrated into tissue microanatomy, tracing stromal components during the organogenesis and remodeling of SLOs is a suitable system for studying the specialization and diversification of mesenchymal cells via close interaction with lymphoid or myeloid cells. BLS12 cells will be a unique and highly valuable tool for exploring the cytological and biochemical nature of lymphoid stromal cells.

Acknowledgments

We thank W. C. Greene for NIK cDNA, A. G. Farr for anti-gp38 Ab, M. D. Cooper for anti-BP-3 Ab, M. H. Kosco-Vilbois for anti-FDC-M2 Ab, and T. Gonda-Ohfiji, K. Araki, and T. Hayashi for technical assistance.

Disclosures

The authors have no financial conflict of interest.

References

1. Fu, Y. X., and D. D. Chaplin. 1999. Development and maturation of secondary lymphoid tissues. *Annu. Rev. Immunol.* 17: 399–433.
2. Gretz, J. E., A. O. Anderson, and S. Shaw. 1997. Cords, channels, corridors, and conduits: critical architectural elements facilitating cell interactions in the lymph node cortex. *Immunol. Rev.* 156: 11–24.
3. Katakai, T., T. Hara, J. H. Lee, H. Gonda, M. Sugai, and A. Shimizu. 2004. A novel reticular stromal structure in lymph node cortex: an immuno-platform for interactions among dendritic cells, T cells, and B cells. *Int. Immunol.* 16: 1133–1142.
4. Katakai, T., T. Hara, M. Sugai, H. Gonda, and A. Shimizu. 2004. Lymph node fibroblastic reticular cells construct the stromal reticulum via contact with lymphocytes. *J. Exp. Med.* 200: 783–795.
5. Gretz, J. E., C. C. Norbury, A. O. Anderson, A. E. Proudfoot, and S. Shaw. 2000. Lymph-borne chemokines and other low molecular weight molecules reach high endothelial venules via specialized conduits while a functional barrier limits access to the lymphocyte microenvironments in lymph node cortex. *J. Exp. Med.* 192: 1425–1440.
6. Sixt, M., N. Kanazawa, M. Selg, T. Samson, G. Roos, D. P. Reinhardt, R. Pabst, M. B. Lutz, and L. Sorokin. 2005. The conduit system transports soluble antigens from the afferent lymph to resident dendritic cells in the T cell area of the lymph node. *Immunity* 22: 19–29.
7. Cyster, J. G. 1999. Chemokines and cell migration in secondary lymphoid organs. *Science* 286: 2098–2102.
8. Cyster, J. G., K. M. Ansel, K. Reif, E. H. Ekland, P. L. Hyman, H. L. Tang, S. A. Luther, and V. N. Ngo. 2000. Follicular stromal cells and lymphocyte homing to follicles. *Immunol. Rev.* 176: 181–193.
9. Luther, S. A., H. L. Tang, P. L. Hyman, A. G. Farr, and J. G. Cyster. 2000. Coexpression of the chemokines ELC and SLC by T zone stromal cells and deletion of the ELC gene in the *plt/plt* mouse. *Proc. Natl. Acad. Sci. USA* 97: 12694–12699.
10. Nishikawa, S., K. Honda, P. Vieira, and H. Yoshida. 2003. Organogenesis of peripheral lymphoid organs. *Immunol. Rev.* 195: 72–80.
11. Mebius, R. E. 2003. Organogenesis of lymphoid tissues. *Nat. Rev. Immunol.* 3: 292–303.
12. Kiyono, H., and S. Fukuyama. 2004. NALT- versus Peyer's-patch-mediated mucosal immunity. *Nat. Rev. Immunol.* 4: 699–710.
13. Eberl, G. 2005. Inducible lymphoid tissues in the adult gut: recapitulation of a fetal developmental pathway? *Nat. Rev. Immunol.* 5: 413–420.
14. Mebius, R. E., and G. Kraal. 2005. Structure and function of the spleen. *Nat. Rev. Immunol.* 5: 606–616.
15. Mebius, R. E., P. Rennert, and I. L. Weissman. 1997. Developing lymph nodes collect $CD4^+CD3^-$ $LT\beta^+$ cells that can differentiate to APC, NK cells, and follicular cells but not T or B cells. *Immunity* 7: 493–504.
16. Yoshida, H., K. Honda, R. Shinkura, S. Adachi, S. Nishikawa, K. Maki, K. Ikuta, and S. I. Nishikawa. 1999. IL-7 receptor α^+ $CD3^-$ cells in the embryonic intestine induces the organizing center of Peyer's patches. *Int. Immunol.* 11: 643–655.